

**UNIVERSIDADE DE SÃO PAULO
INSTITUTO DE FÍSICA DE SÃO CARLOS**

Guilherme Tomishiyo Teixeira de Sousa

**Thinning effects in the simulation of muon production
profiles**

São Carlos

2016

Guilherme Tomishiyo Teixeira de Sousa

**Thinning effects in the simulation of muon production
profiles**

Dissertation presented to the Graduate Program in Physics at the Instituto de Física de São Carlos, Universidade de São Paulo, to obtain the degree of Master in Science.

Concentration area: Basic Physics

Advisor: Prof. Dr. Luiz Vitor de Souza Filho

**Corrected version
(Original version available on the Program Unit)**

**São Carlos
2016**

AUTHORIZE THE REPRODUCTION AND DISSEMINATION OF TOTAL OR PARTIAL COPIES OF THIS THESIS, BY CONVENCIONAL OR ELECTRONIC MEDIA FOR STUDY OR RESEARCH PURPOSE, SINCE IT IS REFERENCED.

Cataloguing data reviewed by the Library and Information Service
of the IFSC, with information provided by the author

Sousa, Guilherme Tomishiyo Teixeira de
Thinning effects in the simulation of muon
production profiles / Guilherme Tomishiyo Teixeira
de Sousa; advisor Luiz Vitor de Souza Filho -
reviewed version -- São Carlos 2016.
75 p.

Dissertation (Master's degree - Graduate Program
in Basic Physics) -- Instituto de Física de São
Carlos, Universidade de São Paulo - Brasil , 2016.

1. Extensive air showers. 2. Thinning. 3. Muon
production profile. 4. Cosmic rays. 5. Astroparticle
physics. I. Souza Filho, Luiz Vitor de, advisor. II.
Title.

*Dedicated to my parents,
the greatest supporters of my scientific life.*

ACKNOWLEDGEMENTS

This work was only possible due to innumEROUS contributions, both at the professional and at the personal level, from many different people. I would like to thank them all.

First, I would like to thank my family. My mother, my father and my brother, Michèle, Paulo and Luigi, for all advices, support and personal assistance, as well as my grandmother Ilza and my uncle Fernando. Without you, I would be lost. Thank you!

Second, to my supervisor, Vitor Souza, for his good will and diligence with my work. Thirdly, to my colleagues and now friends, their endless patience, advices and disposition to explain and teach. I would like to thank Raul Prado, for being almost a second advisor, Rodrigo Lang and Milena Carvalho for all their help with computer related problems as well as core suggestions to my work.

Finally, to all my friends: I feel joyfull for realizing, at the moment of this writting, that they are too numerous to be cited without the risk of committing an injustice by forgetting someone. Regardless, you are all in my heart, thank you so much for all the support and for believing in me more than I believe myself.

“Computers are like Old Testament gods; lots of rules and no mercy.”
Joseph Campbell.

ABSTRACT

SOUZA, G. T. T. de **Thinning effects in the simulation of muon production profiles.** 2016. 75p. Dissertation (Master in Science) - Instituto de Física de São Carlos, Universidade de São Paulo, São Carlos, 2016.

Extensive air showers' (EAS) observables sensible to primary cosmic ray mass are a valuable asset in constraining competing astrophysical and particle physics scenarios proposed both to explaining cosmic rays features, such as their all-particle spectra, as well as their origin. These observables, however, need to be interpreted by comparison to EAS simulations, which are a source of great uncertainty. Shower simulations need to rely on a technique called thinning, an algorithm created to reduce computing time and storage requirement. In this work, we evaluate the effects of thinning over the muon production profile of an EAS simulation. For heavier particles it appears that thinned showers generate profiles with a deeper maximum, while results were not conclusive for protons and photon primaries. We investigate the thinning technique by constructing a toy model for shower simulations in which we have full control of the thinning implementation. To that end, we parameterized the energy distribution and particle production multiplicity from proton-air interactions and proton-pion interactions. However, we find that thinning effects over our model were too severe, rendering it impossible to draw further conclusions about its effects on full air showers simulations.

Keywords: Extensive air showers. Thinning. Muon production profile. Cosmic rays.

RESUMO

SOUZA, G. T. T. de **Efeitos do thinning na simulação de perfis de produção de mísseis**. 2016. 75p. Dissertação (Mestrado em Ciências) - Instituto de Física de São Carlos, Universidade de São Paulo, São Carlos, 2016.

Observáveis sensíveis à composição de raios cósmicos primários em chuveiros atmosféricos extensos são um recurso valioso na construção de cenários competitores em astrofísica e física de partículas, propostos tanto para explicar características dos raios cósmicos, como o espectro de energia de todas as partículas, quanto sua origem. Estes observáveis, no entanto, precisam ser interpretados por comparação a simulações de chuveiros atmosféricos, que constituem fonte de grandes incertezas. Simulações de chuveiros são dependentes de uma técnica chamada thinning, um algoritmo criado para reduzir o tempo de computação e exigências de armazenamento. Neste trabalho, nós avaliamos os efeitos do thinning sobre o perfil de produção de mísseis em uma simulação de chuveiro atmosférico. Para partículas mais pesadas, aparentemente, chuveiros sujeitos ao thinning geram perfis com máximos mais profundos, e para prótons e fótons nossas análises foram inconclusivas. Nós investigamos a técnica do thinning construindo um simulador de chuveiros simplificado, em que o total controle sobre a implementação do thinning é garantido. Para este fim, parametrizamos a distribuição de energia e a multiplicidade de partículas em interações de próton com o ar e de píons com o ar. Entretanto, descobrimos que o efeito do thinning sobre o nosso modelo era muito severo, tornando impossível concluir seus efeitos sobre simulações completas.

Palavras-chave: Chuveiros atmosféricos extensos. Thinning. Perfil de produção de mísseis. Raios cósmicos.

LIST OF FIGURES

Figure 1 – All particle energy spectrum as measured by multiple space and ground experiments.	20
Figure 2 – Energy spectrum for groups of elements as calculated by the model proposed by Sveshnikova (open symbols) and the <i>polygonato</i> phenomenological model. Solid line represents the measured all-particle spectrum.	21
Figure 3 – The Hillas Plot: maximum achievable energy for a source candidate of typical dimensions L and magnetic field B ; b_s is the particle velocity in units of the speed of light	23
Figure 4 – Relative abundance of elements as a function of the nuclear charge Z at energies about 1 GeV/n. Abundances are normalized such that Si=100.	24
Figure 5 – $\langle X_{max} \rangle$ as a function of energy between 10^{18} eV and 10^{20} as measured by the Auger Collaboration (a) and the Telescope Array Collaboration (b), compared to predictions for a pure proton composition (red lines) and pure iron composition (blue lines) for different high energy hadronic interaction models.	25
Figure 6 – (a) A vertical, symmetric shower; (b) An inclined shower defines an early zone and a late zone, where electromagnetic particles are more attenuated; (c) As the zenith angles increases, the assymetry amplifies.	25
Figure 7 – $(\sec \theta)_{max}$ as a function of the primary particle energy and distance from shower core, as expected from simulations softwares for a pure proton (iron) composition in red (blue) lines; data points measured by the Pierre Auger Collaboration.	26
Figure 8 – A typical structure of an EAS initiated by a proton primary.	28
Figure 9 – The number of electrons as a function of the slant depth. Displayed in blue is the total profile generated by a 10^{19} eV proton, and the multiple sub-showers that add up to the total.	29
Figure 10 – Particle densities as a function of shower core distance, as simulated for a 10^{19} eV proton shower.	29
Figure 11 – A schematic view of a pure electromagnetic shower (a) and a hadronic shower (b), as described by the Heitler-Matthews model.	31
Figure 12 – Distribution of longitudinal momentum as a function of the Feynman $x_F \equiv 2p_{ }/\sqrt{s}$, for secondary particles (a) and leading particles (b). The peak at large Feynman x_F is due to diffractive interactions.	35

Figure 13 – Total charged multiplicity (a) and energy distribution (b) as a function of pseudorapidity $\eta \equiv -\ln(\tan(\theta/2))$, according to multiple hadronic interaction model predictions (curves) and accelerators data (points). Data from the 7 TeV collision is from the first LHC run.	37
Figure 14 – Schematic representation of the thinning algorithm. Each vertex represents an interaction. The line width represents the weight of the tracked particles.	38
Figure 15 – RMS deviations from unity of $S(600)/S(600)_{\text{no thinning}}$ (blue symbols), $\rho_\mu(1000)/\rho_{\text{no thinning}}$ (red symbols) and $X_{\max}/X_{\max, \text{no thinning}}$ (green symbols). The “no thinning” subscript denotes quantities reconstructed for a 10^{18} eV proton shower with no applied thinning, while the other quantities are average reconstructions from sets of simulated showers with the various thinning levels. “Opt -5” denotes thinning factor 10^{-5} with weight limitations and MS denotes multisampling.	40
Figure 16 – Pierre Auger Observatory map. The green lines represent the field of view of each one of the 27 telescopes. The names in yellow at the border of the array are the buildings where the telescopes are hosted. XLF and CLF are lasers used for calibration of the fluorescence detectors.	42
Figure 17 – The muon production profile as simulated for 100 showers for proton (iron) primaries in red (blue) curves.	43
Figure 18 – X_{\max}^μ distribution for 1000 simulated proton and iron showers using CORSIKA-75000 code. High energy model of choice was QGSJETII04	43
Figure 19 – Geometry used to obtain the muon traveled distance the time delay.	44
Figure 20 – Evolution with energy of $\langle X_{\max}^\mu \rangle$ as measured by the Auger Collaboration (black dots) and predictions from shower simulations using QGSJETII-04 (solid lines) and EPOS-LHC (dotted lines), for a pure proton (iron) composition in red (blue).	45
Figure 21 – X_{\max} and X_{\max}^μ data converted to the mean logarithmic mass, $\langle \ln A \rangle$, compared to QGSJETII-04 (a) and EPOS-LHC (b) predictions.	45
Figure 22 – Muon production profiles simulated with CORSIKA , for a maximum weight of 10^4 and proton primaries. The red line represents a second order polynomial fit used to extract the position of $X_{\max}^{\mu-\text{sim}}$ (see text).	48
Figure 23 – Muon production profiles simulated with CORSIKA , for a maximum weight of 10^4 and carbon primaries. The red line represents a second order polynomial fit used to extract the position of $X_{\max}^{\mu-\text{sim}}$ (see text).	49
Figure 24 – Muon production profiles simulated with CORSIKA , for a maximum weight of 10^4 and iron primaries. The red line represents a second order polynomial fit used to extract the position of $X_{\max}^{\mu-\text{sim}}$ (see text).	50

Figure 25 – Muon production profiles simulated with CORSIKA , for a maximum weight of 10^4 and photon primaries. The red line represents a second order polynomial fit used to extract the position of $X_{max}^{\mu-sim}$ (see text).	51
Figure 26 – $X_{max}^{\mu-sim}$ as a function of thinning factor for proton simulated showers (a) and iron and carbon simulated showers (b). Values in (b) are normalized by $X_{max}^{\mu-sim}$ at the maximum thinning factor admitted for that particular primary (10^{-3} for iron, 10^{-4} for carbon). Maximum weight was set to 10000, both for electromagnetic and hadronic particles. In (a) points were artificially displaced along the horizontal axis so that the error bars do not overlap.	52
Figure 27 – Charged pion multiplicity in proton-nitrogen collisions as generated by CRMC code for energies 10^7 , 10^9 and 10^{11} GeV.	54
Figure 28 – Energy distribution of pions generated in proton-nitrogen collisions, for energies of 10^7 (a), 10^8 (b) and 10^{11} GeV.	55
Figure 29 – Multiplicity distributions in pion-nitrogen collisions for energies of 4×10^5 (a), 2×10^6 (b), 6×10^7 (c) and 6×10^9 GeV. The red line is the proposed fit (see text).	56
Figure 30 – Evolution with energy of the slope parameter of the exponential function used as parameterization of the multiplicity distribution. In red is a fitted power-law function. The fitted function is a power-law $1.35(E/\text{GeV})^{-0.29}$	57
Figure 31 – Energy distribution of generated pions in pion-nitrogen collisions for energies of 8×10^4 (a), 4×10^7 (b), 4×10^8 (c) and 8×10^{10} GeV (d).	58
Figure 32 – The energy evolution of the fitting function parameters proposed to describe the pion energy distribution in a pion-nitrogen collision. Red curves are the proposed parameterization of the evolution. P_1 was fitted with all parameters free; P_3 was fitted with P_2 free and P_1 fixed, and P_2 was fitted with P_1 and P_3 fixed.	59
Figure 33 – Hadronic interaction inelastic cross-section as a function of the lab momentum p and corresponding parameterization $A \log(p) + B$, shown as the red curve.	60
Figure 34 – Muon production profile as generated in the toy model, with thinning factors of 0 (a), 10^{-6} (b), 10^{-5} (c) and 10^{-4} (d). The red curves are second order polynomial fits used to extract $X_{max}^{\mu-sim}$. Profiles were generated for a 10^9 GeV proton at a 65° zenith angle.	62
Figure 35 – Sample profiles simulated in an event-to-event basis with CORSIKA , (a) and (b) and taking the average of 100 profiles (c) and (d).	64

CONTENTS

1	COSMIC RAYS	19
1.1	Energy Spectrum	19
1.1.1	Knee	20
1.1.2	Ankle	21
1.1.3	Flux suppression	21
1.2	Sources	22
1.3	Composition	23
2	EXTENSIVE AIR SHOWERS	27
2.1	General description	27
2.2	The Heitler-Matthews Model	31
2.3	Hadronic interaction models overview	34
2.4	Thinning	37
2.5	Extensive Air Showers Detection	40
2.5.1	Ground detectors	41
2.5.2	Atmospheric Fluorescence Detectors	41
2.5.3	The Pierre Auger Observatory	42
2.6	The Muon Production Profile	43
3	THINNING EFFECTS IN THE MUON PRODUCTION PROFILE	47
3.1	Differences from the Pierre Auger Collaboration Analysis	47
3.2	Effects on CORSIKA profiles	48
3.3	Parameterization	52
3.4	Toy model and discussion	57
4	CONCLUSIONS	63
	REFERENCES	67

1 COSMIC RAYS

More than a hundred years have passed since the discovery of cosmic rays by Victor Hess (1), and they still pose a challenge for international scientific enterprises. The features of the all-particle energy spectrum are still debated, the astrophysical sources are still unclear, and there are enduring uncertainties about the mass composition of the highest energy particles. Above PeV energies, the cosmic ray flux is too low for direct detection, at least on a statistically significant basis, and one needs to rely on indirect measurements by studying extensive air showers: a particle cascade caused by the cosmic ray interaction with Earth's atmosphere. The shower observables, however, can only be interpreted by comparison with the result of Monte Carlo simulation softwares. But these softwares rely on hadronic high energy interaction models, which are tuned for accelerator data and extrapolated in many orders of magnitudes in energy so as to reach cosmic rays energies.

In this chapter, we present the cosmic ray all-particle energy spectrum in section 1.1. Next, some astrophysical scenarios for the origin of the cosmic rays are discussed in section 1.2. Finally, current knowledge about mass composition is discussed in section 1.3.

1.1 Energy Spectrum

Cosmic rays span a wide energy spectrum: the lower end of the spectrum comprises particles with hundreds of MeV, while the upper end contains particles with hundreds of EeV, the most energetic particles known to modern science. The flux can be so high as one particle per square meter per second, in the MeV regime, or as low as one particle per square kilometer per year, in the EeV regime, yielding more than 30 orders in flux magnitude.

Figure 1 displays the cosmic ray all-particle spectrum as measured by multiple experiments. Cosmic ray experiments can be airborne (or space borne) or ground based, depending upon the energy range of interest. At $E \sim 1$ PeV the flux is too low for direct detection, so experiments measure extensive air shower's observables and interpret them in terms of the primary particle properties.

In a first approximation, the all-particle spectrum can be described as a power law. In Figure 1, however, the flux is multiplied by $E^{2.6}$ in order to make salient the existence of some structures.

The first structure, called the knee, is located about 4 PeV and has been confirmed by multiple experiments, such as Yakutsk (3), Akeno (4) and KASCADE. (5) At about 400 PeV a similar structure, the second knee, can be seen. (6)

At about 5×10^{18} eV a third structure, the ankle, can be found. Its existence has

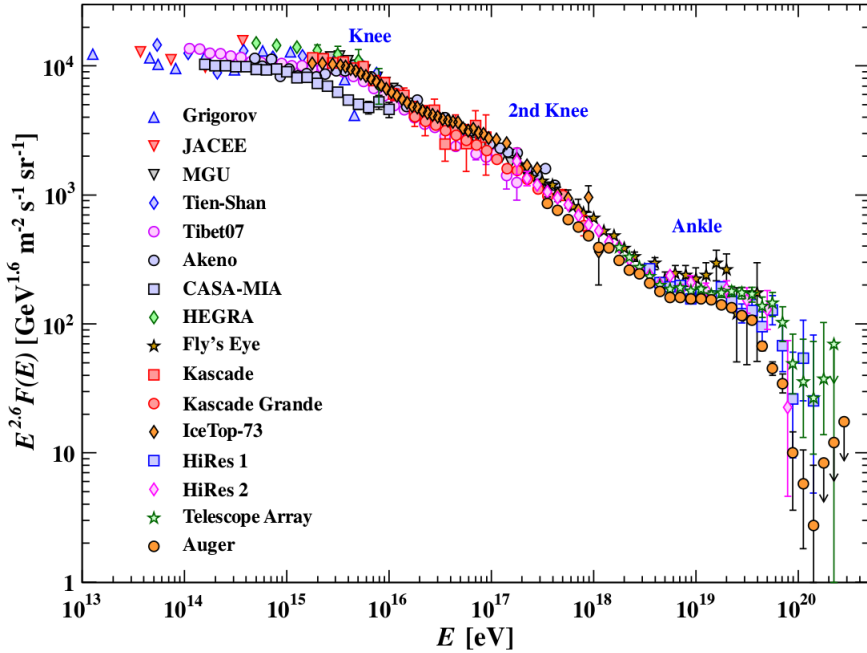


Figure 1 – All particle energy spectrum as measured by multiple space and ground experiments.
Source: OLIVE (2)

been established by the Auger Collaboration (7) and the HiRes experiment. (8)

Finally, a strong suppression can be seen around $10^{19.3}$ eV. The Auger Collaboration (9), as well as the Telescope Array Collaboration (10) are in agreement about its existence.

1.1.1 Knee

If the energy spectrum is understood as a power law $dN/dE \sim E^{-\gamma}$, then the knee can be described as a change in the spectral index γ . The spectrum steepens from a spectral index $\gamma \approx 2.7$ to $\gamma \approx 3.1$. (11)

Concerning the causes of the structure, two classes of explanation can be found in the literature: astrophysical explanations and particle physics explanations. The former explains the structure as an intrinsic feature of the cosmic ray spectrum, while the latter explains it as being due to cosmic rays interactions with Earth's atmosphere.

Astrophysical explanations refers to the acceleration process (11–16), propagation effects (17, 18) and interaction with background particles. (19–21)

Particle physics explanations involve energy transference to “invisible secondaries” as gravitons or supersymmetric particles during extensive air shower development in the atmosphere. (22, 23)

Current evidence seems to favor the knee as being caused by the galactic proton cut-off, as illustrated in Figure 2, but there is not much constrain coming from experiments to settle the question.

1.1.2 Ankle

The ankle can be described as a hardening of the spectrum, or in terms of the spectral index, a regressive to $\gamma \approx 2.7$. The current understanding of the ankle is that it is the result of the transition from galactic to extra-galactic cosmic ray flux (24–27), however the details of this transition are object of controversy. Some models consider that both the galactic and extragalactic components contribute equally to the total flux, with the extragalactic component having a pure proton composition (28,29), while others claim that the transition begins earlier in the spectrum, between 10^{17} and 10^{18} eV, and the ankle signs the end of this transition. (30–32)

A second set of models considers the ankle to be caused by the interaction between extragalactic protons and Cosmic Microwave Background (CMB) photons by means of electron-positron pair production. (25,33–35)

As with the knee, further experimental constraints are needed to establish a favoured model.

1.1.3 Flux suppression

The suppression located at about 3×10^{19} eV is commonly referred as the GZK suppression, due to the predictions of Greisen (36), Zatsepin and Kuzmin (37) of a flux suppression in the cosmic ray spectrum caused by the interaction of cosmic rays with

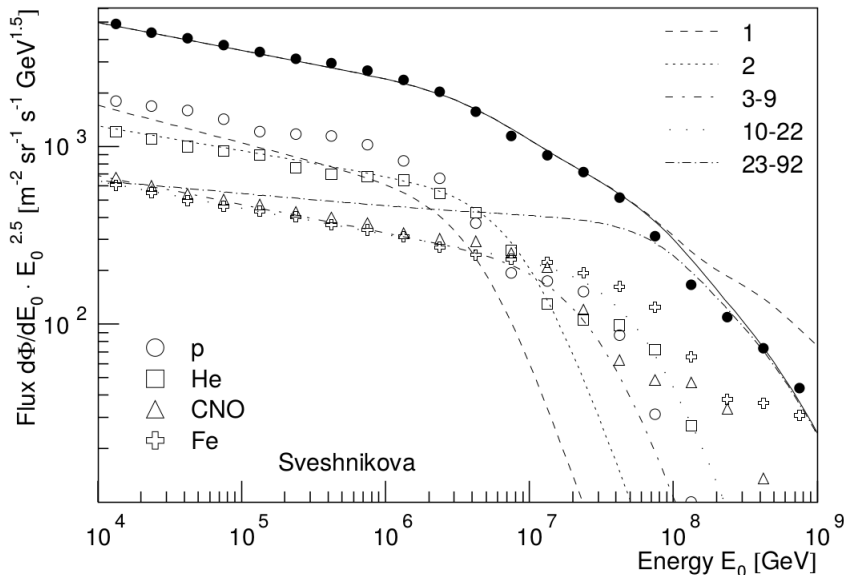


Figure 2 – Energy spectrum for groups of elements as calculated by the model proposed by Sveshnikova (14) (open symbols) and the *poly-gonato* phenomenological model. Solid line represents the measured all-particle spectrum.

Source: HÖRANDEL (11)

CMB photons. (25, 33–35) In this case, protons would lose energy by means of pion photoproduction and heavier nuclei would suffer spallation due to photo-desintegration, turning into smaller nuclei. The effect would restrict high energy cosmic rays to Earth’s cosmological vicinity.

Another natural explanation, however, would be to observe the suppression as a result of the maximal achievable energy in the cosmic rays sources. (26, 27), (30, 35) Recently, spectrum and composition analyses seems to favour the second explanation. (38)

1.2 Sources

The origin of the cosmic rays, specially the ultra-high energy cosmic rays ($E \geq 10^{18}$ eV) is still a mystery to a large extent. Cosmic rays in the GeV energy most likely have a solar origin: this is known due to composition analyses and their distribution in the sky. (39) Galactic cosmic rays, up to 1 PeV in energy, are likely produced in supernova remnants (SNRs) by diffusive shock acceleration, a claim which is substantiated by Fermi Large Area Telescope observation of pion’s decay signature in SNRs (40), among other indirect arguments, such as being a good explanation to the cosmic ray energy spectrum features.

Two types of models are promptly identifiable in the literature concerning UHECRs origin: *top-down* models (41, 42), which propose that cosmic rays are generated by decays of very heavy particles born in the early primordial universe , and *bottom-up* models (43), which try to explore processes capable of accelerating particles up to the very-high energy regime. Since top-down models predict a large number of high-energy photons and current experimental data set a low upper limit for high-energy photon flux (44, 45), they are strongly disfavored.

Bottom-up models rely on either one shot acceleration mechanisms, where particles are accelerated to high energies due to extended electric fields produced by rapidly rotating magnetized objects such as neutron stars; or diffusive shock acceleration, based on the Fermi mechanism. (47)

For a given source, it is possible to relate its dimension, magnetic field and maximum achievable energy, thanks to a calculation proposed by Hillas. (48) Figure 3 shows multiple source candidates. The diagonal solid (dotted) line represents the combination of length dimension and magnetic field required for a source candidate to accelerated a proton (iron) up to 10^{20} eV. The most promising candidates for UHECRs sources are active galaxy nuclei (AGNs), gamma-ray bursts (GRBs) and radio galaxy hot spots.

At the UHE regime, particles are expected to have high magnetic rigidities, and since their sources must be situated in the cosmological vicinity of Earth (< 500 Mpc) due to the GKZ effect, it is possible that UHECRs arrival direction distribution in the sky show

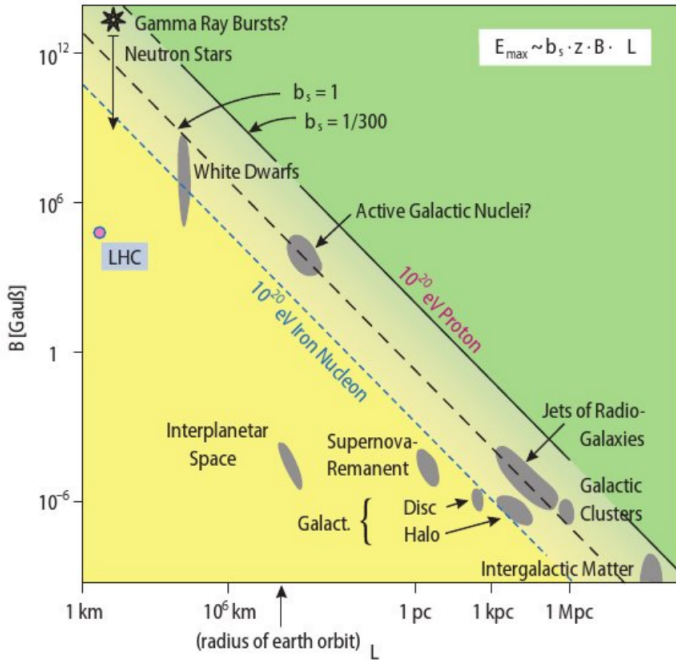


Figure 3 – The Hillas Plot: maximum achievable energy for a source candidate of typical dimensions L and magnetic field B ; b_s is the particle velocity in units of the speed of light.

Source: ZAMORANO (46)

some anisotropy pointing to a source. The Pierre Auger Collaboration has an excellent angular resolution of about 1 degree at the highest energies, making feasible the search for point-like sources. While there were some indications of correlation of arrival directions and the location of the radio galaxy Centaurus A (49–51), a more recent analysis claims that there is no statistically significant evidence of anisotropy. The same study found no correlation in larger scales, such as the galactic plane or the super-galactic plane. (52) The lack of anisotropy is remarkable, and could be understood either by particles with large charges being isotropized by large magnetic fields, or by a high density of sources.

1.3 Composition

Regarding nuclear mass composition, there is a decreasing knowledge with increasing energy: as direct detection is not feasible on a statistically significant basis at energies $> 10^{15}$ eV, the composition can only be studied by means of air showers observables, and can only be evaluated on average for a series of events.

Below and at GeV energies the composition can be very precisely determined, and even individual isotopes can be detected by means of airborne and space experiments (54, 55). At TeV energies individual elements can be identified and at the knee energies ($\sim 10^{15}$ eV) four groups of elements can be measured: hydrogen, helium, CNO and iron. The composition is dominantly hydrogen ($\sim 75\%$), helium ($\sim 24\%$) and traces of other elements, comprising all stable elements of the periodic table ($\sim 1\%$). (56)

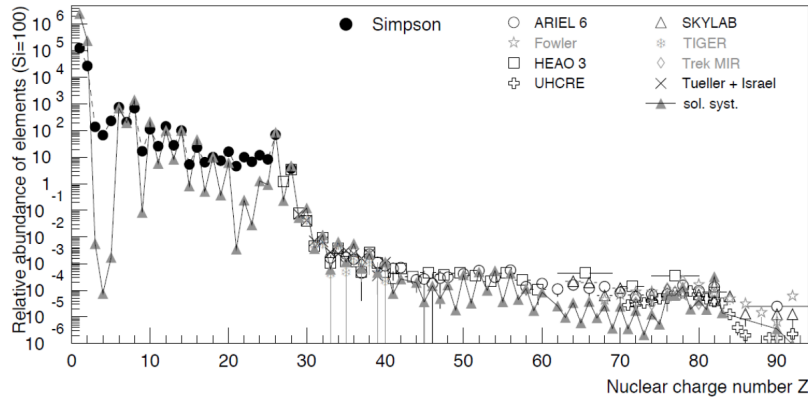


Figure 4 – Relative abundance of elements as a function of the nuclear charge Z at energies about 1 GeV/n. Abundances are normalized such that Si=100.

Source: BLUMER (53)

The cosmic ray relative abundance as a function of their nuclear charge number as measured by several experiments is displayed in Figure 4, together with the composition of the Solar System, at energies of about 1 GeV per nucleon. The two compositions present similar trends, but the dissimilarities are interesting for they reveal information on the acceleration and propagation of cosmic rays.

One exception to the similarity between cosmic ray composition and the Solar System composition is the cosmic ray overabundance of elements in the range $Z = 3 - 5$. It is presumed to be produced by fragmentation of the more abundant particles of the CNO and iron groups during propagation from the source to Earth, a process called spallation. (53) For this reason, they are sometimes called secondary cosmic rays, and the other groups primary cosmic rays. Since the spallation cross section of the relevant nuclei is known at GeV energies, the ratio of secondary to primary cosmic rays can be used to infer the propagation path length of cosmic rays in the Galaxy.

At energies $> 10^{15}$ eV, as was already mentioned, composition can only be studied by means of air showers observables. An energetic cosmic ray that interacts with Earth's atmosphere generates a large number of particles that propagate through the atmosphere, interacting and generating new particles. The number of particles rapidly increases with each generation, until the energy per particle falls to a level at which the probability of attenuation by the atmosphere is comparable to the probability of a new interaction. The atmospheric depth at which this happens is an observable sensible to the primary cosmic ray composition, called the depth of the shower maximum X_{max} .

In Figure 5 it can be seen that measurements made by the Auger Collaboration and the Telescope Array Collaboration show similar trends: $\langle X_{max} \rangle$ increases with shower energy as would be expected by the predictions of computational models for a pure proton composition, for energies up to 5×10^{18} eV. This implies that within this energy range, composition approaches pure proton. Then the trend shifts towards a heavy composition.

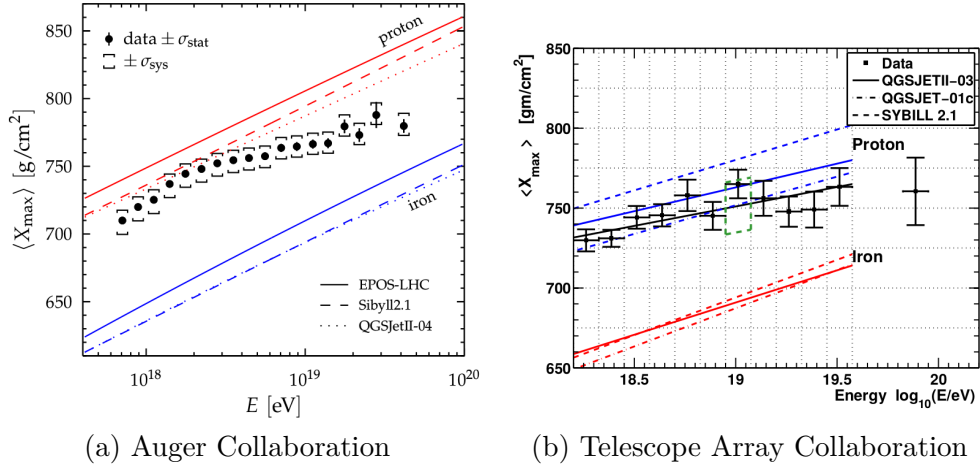


Figure 5 – $\langle X_{max} \rangle$ as a function of energy between 10^{18} eV and 10^{20} as measured by the Auger Collaboration (a) and the Telescope Array Collaboration (b), compared to predictions for a pure proton composition (red lines) and pure iron composition (blue lines) for different high energy hadronic interaction models.

Source: ABBASI (57)

Historically, composition in the very high energy range ($> 10^{19}$ eV) was a source of disagreement: while HiRes (58), Yakutsk (59) and Telescope Array (60) claimed a constant light composition, the Pierre Auger Observatory adjudicated a transition to heavy elements. (61) However, the Auger Collaboration, the Telescope Array Collaboration and the Yakutsk Experiment authored a paper in 2015 were a joint analysis accounting for the different techniques for reconstructing the observables was done. The three experiments now agree that their data are consistent within uncertainties. (57)

The muonic content of an air shower is a rich source of information about the nature of the primary particle. Heavy primary particles produce showers that are abundant in muons, as shall be explained in the next chapter. With this regard there are two quantities useful for investigating the composition of UHE particles: the *risetime asymmetry* and the atmospheric depth in which the production of muons reaches its maximum rate, X_{max}^μ . The latter will be discussed in the next chapter.

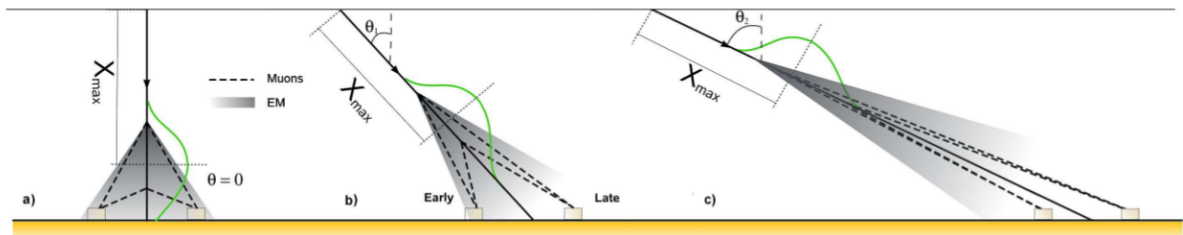


Figure 6 – (a) A vertical, symmetric shower; (b) An inclined shower defines an early zone and a late zone, where electromagnetic particles are more attenuated; (c) As the zenith angles increases, the assymetry amplifies.

Source: DOVA (62)

During their propagation through the atmosphere, muons are less attenuated than electromagnetic particles, such as electrons and photons. As the shower zenith angle increases, the shower front defines an early zone, where the electromagnetic particles are less attenuated, and a latter zone, where the attenuation is intense. If detectors are placed at the ground so as to measure the signal produced by particles traversing it, an asymmetry in the signal is established with respect to detectors in the early zone as opposed to detectors in the late zone. But as the zenith angle increases further, asymmetry is expected to vanish, since electromagnetic attenuation becomes so strong that basically only muons, which are asymmetry free for suffering very low attenuation, reach the ground. This is illustrated in Figure 6. Therefore, for a given primary particle energy, there is an angle where the asymmetry is at its maximum, and one can construct an observable, $(\sec \theta)_{max}$ which is sensitive to the primary particle composition. (62)

The Auger Collaboration has studied the risetime of showers in the UHE regime. In Figure 7 (a) and (b), values of $(\sec \theta)_{max}$ as a function of energy are displayed for distances of 500 – 1000 and 1000 – 2000 m from the shower core, together with predictions from simulation softwares. The results are consistent with the X_{max} and $\sigma(X_{max})$ analyses: the composition gets heavier as energy increases. (63)

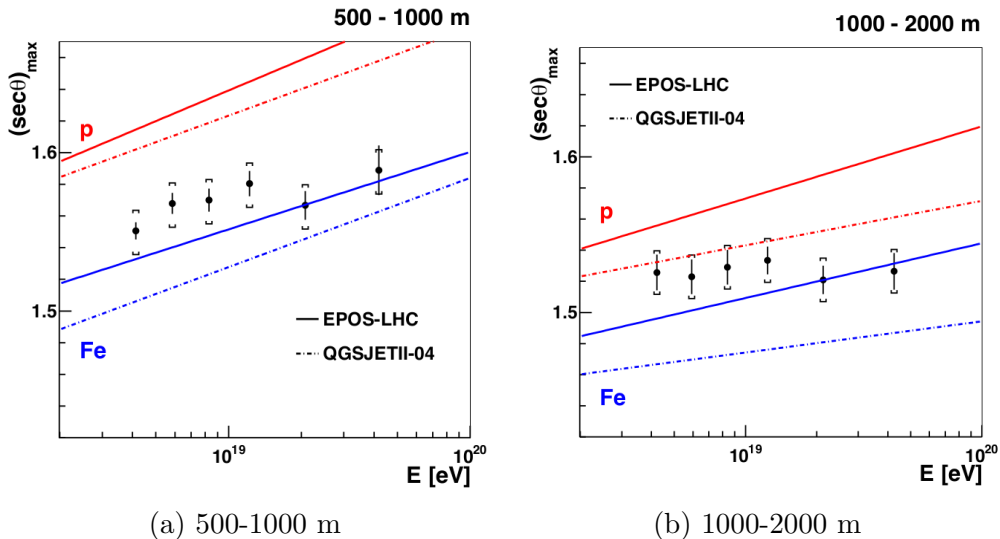


Figure 7 – $(\sec \theta)_{max}$ as a function of the primary particle energy and distance from shower core, as expected from simulations softwares for a pure proton (iron) composition in red (blue) lines; data points measured by the Pierre Auger Collaboration.

Source: AAB (63)

2 EXTENSIVE AIR SHOWERS

When a high energy cosmic ray ($E > 10^{14}$ eV) interacts with Earth's atmosphere, a large number of particles is generated as a consequence of the high energy of the collision's center-of-mass. These secondaries particles propagate through the atmosphere, further interacting and generating new particles or decaying. This process goes on until most particles are either absorbed in the atmosphere or reach the ground, where they can be measured by detectors. This multi-particle process is called an Extensive Air Shower (EAS), a rich and complex phenomenon which will be the subject of this chapter.

Section 2.1 intends to provide a general description of a shower and its main components. In section 2.2 the Heitler-Matthews model is discussed, with the aim of granting a grasp of physical intuition about air shower processes. Section 2.3 briefly overviews the different high energy hadronic interaction models used in air showers simulators. The thinning technique, an algorithm that reduces computing time and storage requirement in air shower simulation is addressed in section 2.4. Section 2.5 discusses air shower detection, with special emphasis on the Pierre Auger Observatory, and finally section 2.6 concludes by presenting the muon production profile, a very important concept for this work.

2.1 General description

As has already been described, an EAS is initiated by a high energy cosmic ray that interacts with Earth's atmosphere nuclei. A fraction of the cosmic ray energy, given by the inelasticity of the collision, is destined to the production of new particles, while the remaining fraction is carried by the leading particle deeper into the atmosphere. The total number of particles generated in an EAS can be very large: it scales with energy, and can be as big as 10^{10} in a shower initiated by a 10^{19} eV cosmic ray proton.

An EAS can be divided into three parts with respect of the types of particle produced, as illustrated schematically in Figure 8. The majority of the particles (more than 99%) are electromagnetic particles: photons, electrons and positrons (for simplification, electrons and positrons are referred only as "electrons"), which are represented by the blue circles in Figure 8. There are three main processes that develop the EM component: electron-positron pair production, bremsstrahlung radiation and energy losses by ionization. The EM component carries the majority of the EAS energy (about 85% of the primary energy).

The theory underlying the EM component is well understood: it can be explained with Quantum Electrodynamic (QED) processes. Heitler was the first to propose a

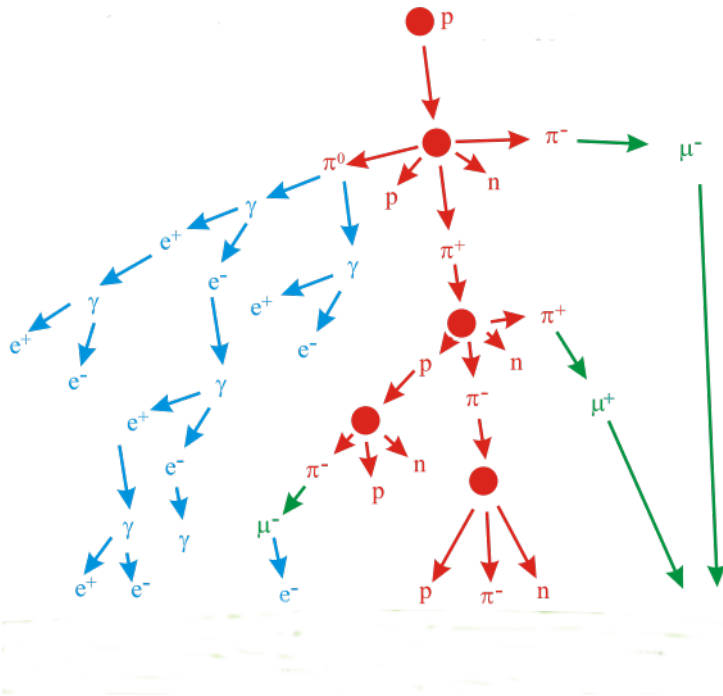


Figure 8 – A typical structure of an EAS initiated by a proton primary.

Source: AIR (64)

comprehensive model in the 1940s. (65) It can also be reliably simulated by several developed softwares, such as EGS (66), FLUKA (67) and Geant. (68)

The majority of particles are in the EM component, but the hadronic component is the main engine behind an EAS, illustrated as the red branch in Figure 8. Hadronic particles comprise: a) charged pions (about 2/3 of the hadronic particles); b) neutral pions (about 1/3) which decay rapidly into photons, feeding the electromagnetic component; c) other hadrons, such as kaons, delta particles, protons and neutrons (very few of them). The theory that best describes the hadronic component is Quantum Chromodynamics (QCD), but the uncertainties are severe, since our knowledge of hadron's collisions at such high energies ($\sqrt{s} >> 100$ TeV) is incomplete. While it is possible to write cascade equations for the hadronic component (69,70), the need for accounting particle decays and the complexity of hadronic multiparticle production renders deriving a set of analytical expressions impossible. Hard collisions (head-on collisions with large momentum transfer) are treatable by perturbative methods, but the soft collisions are not completely understood. The hadronic component is the main shower engine because the majority of photons are generated by π^0 decays ($\pi^0 \rightarrow 2\gamma$), and because charged pion decays generate the final component of the shower: the muonic component.

Muons, represented as the green circles in Figure 8, are generated by pion decays ($\pi^\pm \rightarrow \mu^\pm + \nu_\mu/\bar{\nu}_\mu$), and have an appreciable lifetime, so a great number of them propagates through the atmosphere hitting the ground. The muonic component carries a wealth of

information about the primary particle. More details will be given in section 2.6.

When describing the air shower development, a useful parameter is the atmospheric slant depth, defined by the integration of the atmospheric density from infinity until the referred altitude, or:

$$X = \int_h^\infty \rho(x)dx, \quad (2.1)$$

where $\rho(x)$ is the atmospheric density as a function of the altitude, x .

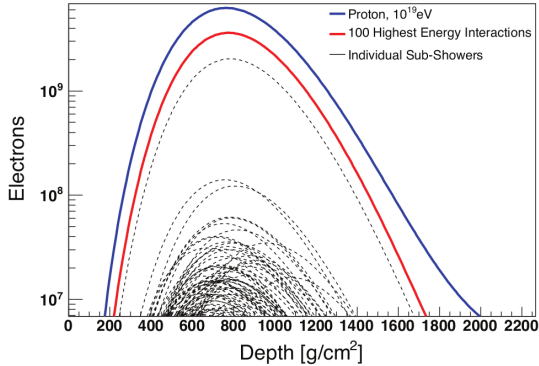


Figure 9 – The number of electrons as a function of the slant depth. Displayed in blue is the total profile generated by a 10^{19} eV proton, and the multiple sub-showers that add up to the total.
Source: ALLEN (71)

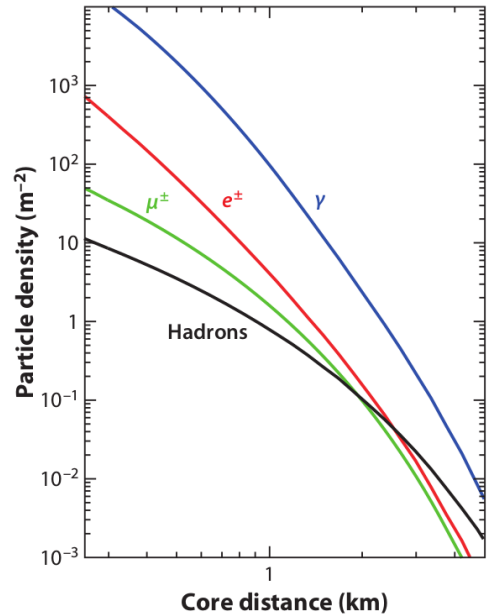


Figure 10 – Particle densities as a function of shower core distance, as simulated for a 10^{19} eV proton shower.
Source: ENGEL (72)

Concerning longitudinal development, three phases can be identified. At first, the mean energy per particle is large, and numerous collisions generate more particles in a cascading process. This is called the growth phase. After multiple collisions, during the phase called shower maximum, the mean energy per particle reaches a value referred as the critical energy - the energy such that the interaction mean free path gets comparable to the absorption mean free path or decay mean free path. At this stage, production of new particles is suppressed. Finally, the number of shower particles attenuates as particles lose energy and get absorbed in the atmosphere, or decay. This last stage is referred as the shower tail. The stages can be identified in Figure 9: growth phases occurs in the range from 0 to 800 g/cm^2 , approximately, with the shower maximum being at 800 g/cm^2 . The tail occurs in the remainder of the atmosphere. Sub-showers are also displayed in the figure, so as to illustrate how they add up to the total profile.

The total number of charged particles at each depth can be derived by solving the shower cascade equations. (73) The profile is usually described by the Gaisser-Hillas function (74):

$$N_e(X) = N_e^{max} \left(\frac{X - X_1}{X_{max} - X_1} \right)^{\frac{X_{max} - X_1}{\lambda}} \exp \left(\frac{X_{max} - X}{\lambda} \right), \quad (2.2)$$

where N_e^{max} is the maximum number of charged particles at X_{max} , the depth of shower maximum, X_1 is the depth of the first interaction and λ is the attenuation length.

The shower also has a lateral development, as illustrated in Figure 10, displaying various particle densities at different shower core distances. Indeed, the spread can be as large as to cover areas of $\sim 20 \text{ km}^2$ for a 10^{19} eV cosmic ray. Electromagnetic particles are scattered by coulombian interactions, while hadronic particles spread due to large transverse momentum generated in hard collisions. Muons, on the other hand, do not scatter significantly, and propagate undisturbed through the atmosphere. This implies that muons retain a memory of their production point, a feature that can be exploited to infer the primary particle composition, as shall be explained in section 2.6.

Low energy electrons scattering distances are given by the Molière radius, which is inversely proportional to the density of the medium ($r_M \approx 80 \text{ m}$ at sea level). (75) This means that close to the shower core, the majority of particles are electromagnetic. The lateral spread of electrons can be described analytically by the Nishimura-Kamata-Greisen (NKG) lateral distribution function (LDF) (76, 77), which provides the particle density at a distance r from the shower core:

$$\rho(r) = \frac{N_e}{2\pi r_M^2} C_s \left(\frac{r}{r_M} \right)^{s-2} \left(1 + \frac{r}{r_M} \right)^{s-4.5}, \quad (2.3)$$

where N_e is the number of electrons generated in the shower, $s \equiv 3X/(X + 2X_{max})$ is a parameter called the shower age and

$$C_s = \frac{\Gamma(4.5 - s)}{\Gamma(s)/\Gamma(4.5 - 2s)}, \quad (2.4)$$

is a normalization constant (with Γ being the gamma function).

As for muons, their spread is considerably larger than that of EM particles. This may seem a contradiction, since it was claimed that muons do not scatter significantly. However, muons are generated by pion decays, and pions get large transversal momentum in hard hadronic collisions ($p_t \sim 350 - 400 \text{ MeV}$). It is possible, as with the EM particles, to describe muon densities at a distance r from the shower core with the Greisen lateral distribution function. (77) Moreover, Greisen derived an empirical formula for all charged

particle densities at a distance from shower core as:

$$\rho(r, N) = \frac{0.4N}{r_M^2} \left(\frac{r_M}{r} \right)^{0.75} \left(\frac{r_M}{r + r_M} \right)^{3.25} \left(1 + \frac{r}{11.4r_M} \right) \quad (2.5)$$

where N is the total number of charged particles. The expression is valid for $0.05 \text{ m} < r < 1500 \text{ m}$ and for atmospheric depths in the range $537 \text{ g/cm}^2 < X < 1800 \text{ g/cm}^2$.

2.2 The Heitler-Matthews Model

While complete Monte Carlo simulations of EAS are possible, the numerical nature of the calculation does not favour physical intuition. In this respect, a simplified analytical model, while not reproducing correctly all features of EAS, may be instructive so as to enlighten key features of it, provided we keep in mind it is no adequate substitute for full simulations.

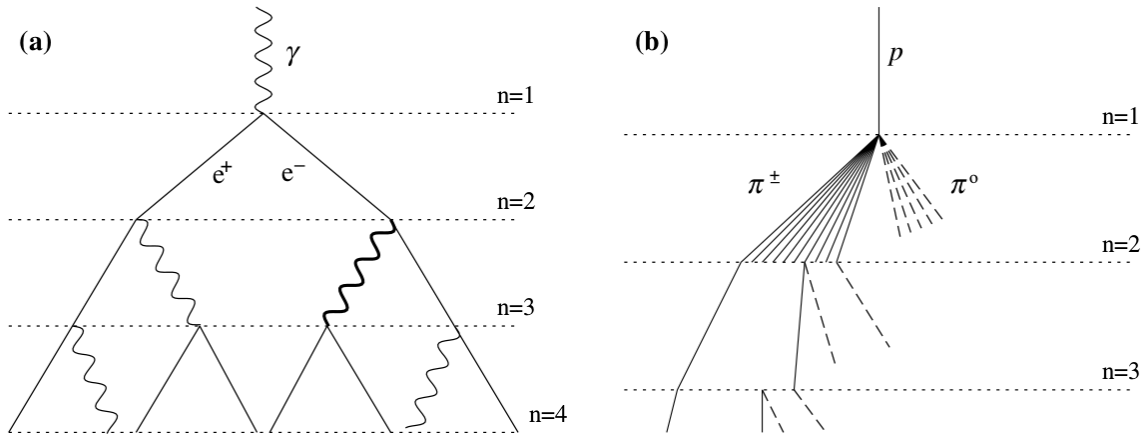


Figure 11 – A schematic view of a pure electromagnetic shower (a) and a hadronic shower (b), as described by the Heitler-Matthews model.

Source: MATTHEWS (78)

We start by considering a pure electromagnetic shower, following the model proposed by Heitler in the 1930s (65), and next we generalize the ideas for a hadronic shower.

In Heitler's model, electrons, positrons (here referred only as electrons) and photons undergo pair-production and bremsstrahlung repeatedly. This always happens to every single particle after they travel a fixed length: the radiation length. Consequently, after n generations, the shower contains 2^n particles, as schematically shown in Figure 11. The process goes on until a critical energy per particle is reached (the energy at which average collisional losses begin to exceed radiative losses), then multiplication is considered to cease abruptly. This simplified picture cannot account for all details of EM showers but we proceed to show that two important features are derivable: the total number of particles

is proportional to the primary particle energy, E_0 , and the depth of shower maximum is proportional to the logarithm of E_0 .

Let $d = \lambda_r \ln 2$ stand for the distance an EM particle propagates before splitting, where λ_r is the radiation length in the medium. After n splitting lengths, the shower size is $N = 2^n = \exp(x/\lambda_r)$ where $x = n\lambda_r \ln 2$. Denoting by ε_c^e the critical energy ($\varepsilon_c^e = 85$ MeV in air (78)), then multiplication comes to a halt when the energy per particle equals ε_c^e . Since particles do not attenuate in this model, this is precisely when the shower reaches its maximum development. If we consider that a photon of energy E_0 is the primary particle, then the following relation must hold:

$$E_0 = \varepsilon_c^e N_{max}. \quad (2.6)$$

This happens at depth X_{max} after n_c splittings. Since $N_{max} = 2^{n_c}$, it follows from Eq.(2.6) that $n_c = \ln(E_0/\varepsilon_c^e)/\ln 2$. Since $x = n\lambda_r \ln 2$, this implies:

$$X_{max}^\gamma = n_c \lambda_r \ln 2 = \lambda_r \ln(E_0/\varepsilon_c^e), \quad (2.7)$$

where the γ superscript is just a reminder of the electromagnetic validity of the equation. Consequently, the elongation rate $\Lambda \equiv dX_{max}/d \log_{10} E_0$, defined as the rate of increase of X_{max} per energy decade, yields $\Lambda = 2.3\lambda_r \approx 85$ g/cm².

As was stated, the model predicts that the total particle number responds linearly to the primary energy, while the depth of shower maximum only logarithmically. Following the model's prediction, the total number of electrons is predicted to approach $N_e \approx (2/3)N_{max}$, but this is way to large, since photons often outnumber electrons by large. An *ad hoc* solution is to postulate the electron numbers as a tenth of the total EM particles, which provides an estimate of the order of magnitude.

Matthews extended Heitler's ideas for hadronic showers. (78) His model predicts a number of important features of EAS:

- The number of muons generated is shown to be $N_\mu \approx 10^4 \left(\frac{E_0}{1 \text{ PeV}} \right)^{0.85}$ for proton showers, while heavier primaries of atomic mass A generates more muons by a factor $A^{0.15}$.
- The shower maximum is predicted to be at $X_{max}^p = (470 + 58 \log_{10}(E_0/1 \text{ PeV}))$ g/cm² for proton primaries, while heavier particles of atomic mass A are off by a factor $\lambda_r \log_{10} A$, with λ_r being the radiation length. This implies that proton and iron initiated showers have a constant separation with respect to the evolution of X_{max} with energy.
- The elongation rate is predicted as $\Gamma^p = 58$ g/cm² per decade, being smaller than in the EM case.

Matthews assumed that each hadronic particle travels a fixed distance of $\lambda_I \ln 2$, where now λ_I is the hadronic *interaction length*, before splitting into N_{ch} charged pions and $\frac{1}{2}N_{ch}$ neutral pions. The neutral pions are assumed to decay immediately rendering EM sub-showers, while charged pions propagate deeper into the atmosphere. Pions further interact splitting into new particles until their energy falls below the critical energy, ε_c^π , when they decay into muons, this happening after n_c interactions. Values are taken as $\lambda_I \approx 120 \text{ g/cm}^2$, which is a good approximation in the range $10 - 1000 \text{ GeV}$, $N_{ch} = 10$ and $\varepsilon_c^\pi = 20 \text{ GeV}$. (78)

The number of muons in the shower is obtained using $N_\mu = (N_{ch})^{n_c}$. After n interactions, the energy per pion is $E_0/(\frac{3}{2}N_{ch})^n$, so that when $n = n_c$, $E_\pi = \varepsilon_c^\pi$ and

$$n_c = \frac{\ln(E_0/\varepsilon_c^\pi)}{\ln\left(\frac{3}{2}N_{ch}\right)} = 0.85 \log_{10}(E_0/\varepsilon_c^\pi). \quad (2.8)$$

Using Eq.(2.8), we can write:

$$\ln N_\mu = n_c \ln N_{ch} = \beta \ln(E_0/\varepsilon_c^\pi), \quad (2.9)$$

or

$$N_\mu = \left(\frac{E_0}{\varepsilon_c^\pi}\right)^\beta \approx 10^4 \left(\frac{E_0}{1 \text{ PeV}}\right)^{0.85}. \quad (2.10)$$

Since the depth of the first interaction is paramount in determining the depth of the shower maximum, a further assumption is made about the former. A parameterization using data from inelastic proton-air cross-section (79) is adopted:

$$X_0 = \lambda_I \ln 2 = (61 \text{ g/cm}^2)(1 - 0.1 \ln(E_0/\text{PeV})) \ln 2. \quad (2.11)$$

The depth of the shower maximum then stems from the first interaction and the EM sub-showers generated at that point with primary energy $E_0/(3N_{ch})$. Applying Eq.(2.7) results in:

$$X_{max}^p = X_0 + \lambda_r \ln[E_0/(3N_{ch}\varepsilon_c^\pi)] = (470 + 58 \log_{10}(E_0/1 \text{ PeV})) \text{ g/cm}^2. \quad (2.12)$$

This calculation clearly underestimates the true value, since it does not account for new electromagnetic showers generated in further neutral pion decays. Nevertheless, the qualitative behavior is correct, and the elongation rate, calculated by differentiating the expression with respect to $\log_{10} E_0$ yields 58 g/cm^2 per decade, which is in good agreement with Monte Carlo shower simulations. (79)

Quantities for heavier primary particles can be derived by using the **superposition model**, which treats a nucleus of atomic mass A and energy E_0 as A individual nucleons

with energy E_0/A . This approximation is reasonable since typical nuclear binding energies are in MeV scale, orders of magnitude lower than the energy of particles that induce air showers. With this approximation in mind, we can exchange $E_0 \rightarrow E_0/A$ in Eqs.(2.12) and (2.10), obtaining

$$N_\mu^A = N_\mu^p A^{0.15}, \quad (2.13)$$

$$X_{max}^A = X_{max}^p - \lambda_r \ln A. \quad (2.14)$$

Since the energy E_0 is distributed in A particles, the shower reaches the critical energy ε_c^π in fewer generations, so less energy gets transmitted to the electromagnetic channels and the shower gets richer in muons. An iron shower will have $(56)^{0.15} = 1.8$ times as many muons as a proton shower of the same total energy. Also, in agreement with Monte Carlo simulations, iron showers do not penetrate as deeply as proton showers for the same total energy.

It is possible to further sophisticate this ideas. Matthews goes on and consider collisions which are not perfectly inelastic, introducing a leading particle effect. Montanus extends the analysis by including all electromagnetic sub-showers and by considering an energy dependence in the interaction length. (80) However, what was outlined is sufficient for providing a superficial understanding about some important shower features.

2.3 Hadronic interaction models overview

In section 2.2 a simplified toy model was presented for describing EAS. A much more powerful option, however, is a full Monte Carlo simulation of the shower.

The main problem with shower simulations is incorporated in the understanding of the hadronic interactions. Quantum chromodynamics, the physical theory underlying these interactions, fails to provide methods for calculation of non-perturbative processes: soft interactions and diffractive interactions, which are very common in EAS. Moreover, collisions in EAS ranges all the way to $\sqrt{s} \sim 400$ TeV, while accelerators have access to a significantly smaller phase space restricted to $\sqrt{s} \sim 14$ TeV. In this way, phenomenological modeling with theoretical constrains are necessary for describing multiparticle production at accelerator energies and corresponding extrapolation to higher energies.

In this section we discuss the general ideas of three hadronic interaction models incorporated in three different softwares: **EPOS** (81), **QGSJET II** (82) and **SIBYLL**. (83–85) Additionaly, there exists the **DPMJET II** (86) and **DPMJET III** (87) softwares, which possess many similarities with **SIBYLL 2.1** and so are not discussed here. The models discussed are high energy interaction models, valid for hadron energies above ~ 200 GeV. From particle-production threshold up to this energies, simulations must be complemented

by softwares incorporating low-energy interaction models. Frequently used ones are the GHEISHA (88), FLUKA (67) and UrQMD (89) softwares.

All high-energy models share a common framework, in considering hadrons to be composed of valence quarks and diquarks (the quantum number carriers), sea quarks and gluons. A hadronic interaction happens when color is exchanged between two hadrons. The color connection resulting from the color exchange between two partons is phenomenologically modeled as a stretched string between them, where the kinetic energy is converted and stored in its field. When this string is fragmented, new hadrons are produced. (90)

The final state is defined by the valence quarks, which typically inherit 50% or more of the momentum of the hadron, and particles produced in the string fragmentation. The valence quark produces a leading particle, since the string-generated particles do not inherit a valence quark or diquark. Indeed, secondary particles have small momentum fractions, while the leading particles typically have a flat distribution, as displayed in Figure 12. The transverse momentum is exponentially distributed around $\langle p_{\perp} \rangle \sim 0.35 - 0.40$ GeV.

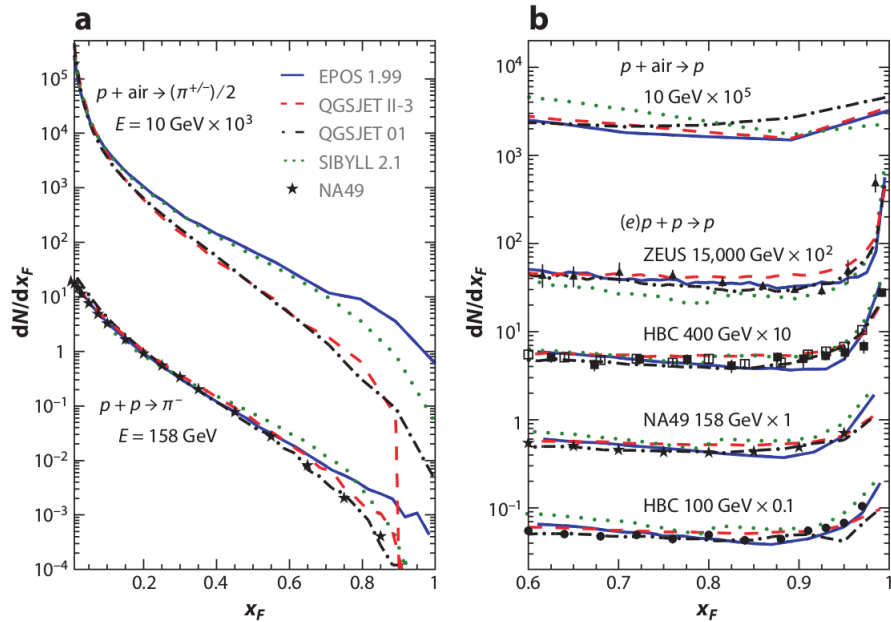


Figure 12 – Distribution of longitudinal momentum as a function of the Feynman $x_F \equiv 2p_{||}/\sqrt{s}$, for secondary particles (a) and leading particles (b). The peak at large Feynman x_F is due to diffractive interactions.

Source: ENGEL (72)

Jets originating from hard interaction, which become progressively more common when $\sqrt{s} > 50$ GeV, can be calculated perturbatively above a minimum transverse momentum $p_{\perp}^{\text{cutoff}}$, provided the parton densities are known. This happens if jet production inclusive cross section scales as $\sigma_{\text{jet}} \sim s^{\Delta} \ln s$ if the gluon parton density scales as $xg(x) \sim x^{-\Delta}$ for small momentum fractions x (91); for $\Delta = 0.3...0.4$, the implication is that the jet inclusive cross section rises faster than the total cross section, giving birth to multiple hard interactions within a same hadron-hadron interaction at high energies. (92) At even

higher energies, parton (constituents of a hadron) density increases and individual wave functions start to overlap, reducing the number of independent partons. This promotes a saturation effect. (93)

In the classic minijet model, such as adopted in **SIBYLL**, the raise in the cross section and secondary particle multiplicity is caused by production of jets with small p_{\perp} ($\sim 2 - 3$ GeV). (94–97) An approach that is more favored by current data (98,99) and more theoretically self-consistent is obtained if one considers the hard minijet cross section to be part of a class of multigluon diagrams. This so-called “semihard Pomeron” (100,101) (a pomeron is a color singlet) approach introduces a virtuality scale, Q_0^2 : particles in the high virtuality regime $|q^2| > Q_0^2$ are treated by perturbative QCD, while a phenomenological soft pomeron amplitude is employed for particles in the soft, low virtuality regime. Total amplitude of a general pomeron is then used as a building block to derive all partial cross sections and probabilities for final states, by means of a theory known as the Gribov-Regge theory. (102) This approach is the choice of both **EPOS** and **QGSJET**.

SIBYLL is the simplest model for air shower simulations. For treatment of parton saturation, the effective transverse area of all partons is compared with that of the mother hadron, in that way determining the region of phase-space prone to saturation. (84) By turning the transverse-momentum cutoff of soft-hard interactions ($p_{\perp}^{\text{cutoff}}$) energy dependent, it turns all the saturation region into the soft domain, where parameterizations are employed.

The **QGSJET** model implements microscopic models of multipomeron interactions and exchanges, leaving only a few parameters to be tuned. It is the model with the least number of free parameters. A detailed theoretical model of pomeron-pomeron interaction is implemented to describe saturation effects (an approach with treats well low virtuality partons, but does nothing for the high-virtuality case. (82))

EPOS is the model that is tuned to describe larger volumes of accelerator data. It is based on a microscopic pomeron model in which the pomeron-parton coupling, including momentum sharing, is explicitly calculated. (103) Baseline predictions are modified by parameterizations in order to improve agreement with data. (81) As for saturation effects, **EPOS** treats them with parameterizations, which have a flexible extrapolation to the ultrahigh energy regime.

Figure 13 displays the model predictions for the charged multiplicity and energy distribution as a function of the pseudorapidity, a quantity which measures the particle’s production angle with respect to the collision direction, before the models were tuned to LHC data. Not remarkably, the disagreements are substantial at high energies.

For an extensive and much more detailed review about hadronic interaction models, see (72) and (104).

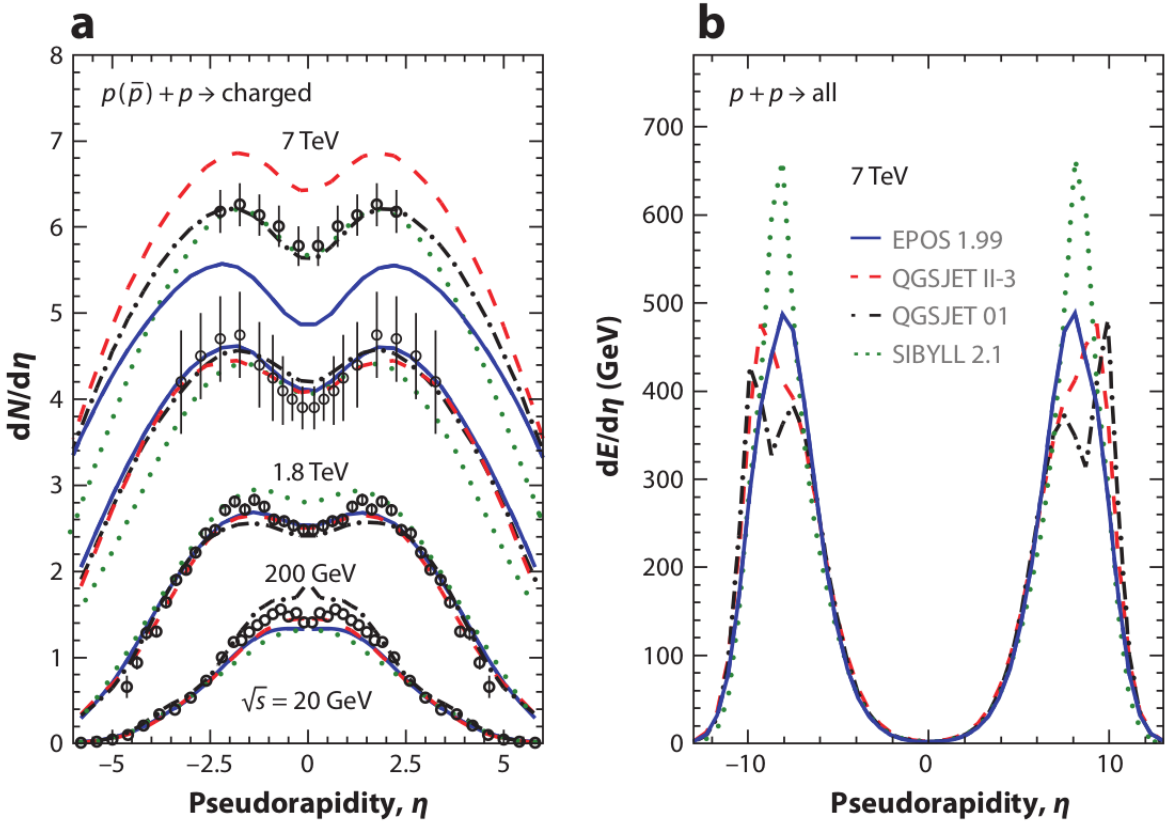


Figure 13 – Total charged multiplicity (a) and energy distribution (b) as a function of pseudorapidity $\eta \equiv -\ln(\tan(\theta/2))$, according to multiple hadronic interaction model predictions (curves) and accelerators data (points). Data from the 7 TeV collision is from the first LHC run.

Source: ENGEL (72)

2.4 Thinning

For all advantages Monte Carlo simulation present, it also costs a lot computationally speaking: the number of particles can be as high as 10^{10} in a 10^{19} eV shower, and it has been argued in 2.2 that particle numbers are expected to scale with energy. This implies that a great amount of processing power and memory storage is required for simulation of high energy showers. While it is possible to fully simulate a shower in the UHE regime (see, for instance, the collection of simulated showers from (105)) it is not possible to do as many simulations as required for statistical studies, a limitation that would exclude simulations from being used in a great number of data analysis.

The thinning is a technique tailored to solve this problem: it is an algorithm that intends to reduce computational time and storage requirement, while keeping artificial fluctuations at minimum. It consists in simulating just a representative subset of particles, assigning them weights so as to keep fluctuations at a minimum.

Thinning technique is based upon a more general tool called Variance Reduction.

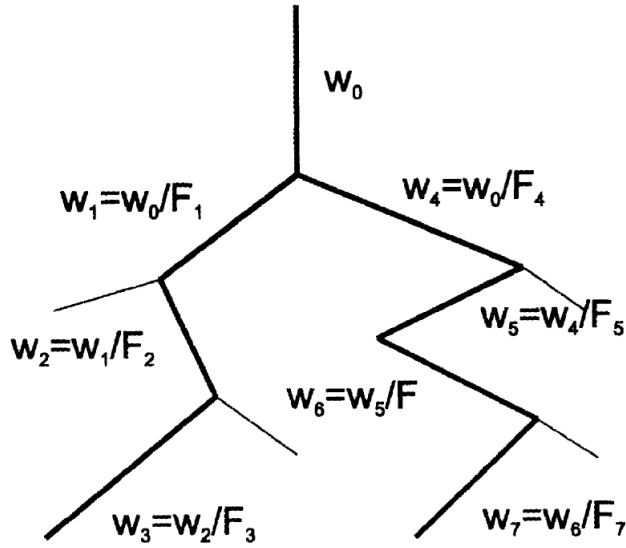


Figure 14 – Schematic representation of the thinning algorithm. Each vertex represents an interaction. The line width represents the weight of the tracked particles.

Source: KOBAL (106)

Variance reduction attempts to reduce the variance of an estimator of a random variable X , without introducing bias. Suppose $X \sim f(X)$ is a randomly distributed variable, $f(X)$ being either the probability distribution function or the probability mass function, according to the discrete or continuous character of X . Suppose $V(X)$ is a random variable with true expectation value θ . Then an unbiased estimator for θ is given by:

$$\hat{\theta} = \int V(x)f(x)dx. \quad (2.15)$$

If $q(X)$ is another PDF, then clearly, if we denoted by $E_q[\cdot]$ the expectation value calculated with the distribution $q(X)$:

$$\hat{\theta} = \int V(x)\frac{f(x)}{q(x)}q(x)dx = \int V(x)w(x)q(x)dx = E_q[V(x)w(x)], \quad (2.16)$$

must hold, which implies that the sampling from the new distribution $q(X)$ does not induce bias in the estimator, as long as the expectation is weighted accordingly. From this it is reasonable to expect that the thinning technique does not induce bias in shower observables.

The algorithm consists in choosing a fraction of the primary energy, the *thinning factor* t_f , which defines an energy scale $E_t = t_f E_0$. During the simulation, if a given particle has an energy greater than the thinning energy, it is simulated normally as if no thinning was in operation. If not, the details depend on the interaction that gave birth to the particle: if all particles in an interaction have an energy below the thinning energy, the algorithm will follow a single particle with probability e/E_{sum} , where e is its energy and

E_{sum} is the sum of the energy of all particles generated in the interaction. To that particle, a weight $w = w_{in}E_{sum}/e$ is attributed, where w_{in} is the weight of the mother particle (unthinned particles have unit weight). If, however, an energetic interaction generates some secondaries with energies below the thinning energy and some above, then one will follow the latter particles and follow a former with probability e/E_t . Again, if a particle with energy $e < E_t$ is followed, a weight $w_{in}E_t/e$ must be designated to it.

The above algorithm is called the Hillas thinning, inspired by Hillas' work in the late 1990s. (107) While containing many resemblances with Hillas' ideas, what was described above is more similar to Kobal's proposal: a different version of the technique, called statistical thinning (106), which is optimized for reconstruction of the shower far from the shower core. It is very similar to the way simulation softwares such as CORSIKA (108) implement the technique. In the same work, Kobal also propose the use of weight limitation, so as to greatly reduce artificial fluctuations. A maximum weight, w_{max} , is chosen: if a given particle, as a result of the thinning algorithm, would be assigned a weight $w > w_{max}$, it is assigned w_{max} instead and it is excluded from subsequent thinning processes, regardless of its energy. Since EM particles vastly outnumber hadronic particles, it is common to assign different thinning parameters for the electromagnetic and the hadronic component. In this way, there is an EM thinning factor, t_f , and a hadronic thinning factor, t_{had} . Maximum weights are also chosen differently for the EM and hadronic component. Also, due to the large number of particles near the shower core, detectors might saturate, rendering the storage of a vast number of particles close to core useless. In that respect, a *radial thinning* can be employed: a radial distance from the shower core, r_{max} , is selected, defining a cone around the core. Particles within a position r inside the cone are kept with probability r/r_{max} , while particles outside the cone are always kept. The weight of a particle kept by this process must be scaled by a factor r_{max}/r .

A different problem is to simulate the flux a detector at the ground would detect. For that end, a resampling procedure can be adopted. (109) Resampling consists in choosing an area A_{sr} around a given detector, small enough to represent well densities in the parameter space, but not too small as to induce artificial fluctuations. Next, for each incoming particle reaching the ground, an effective area, A_d is calculated: A_d is the area of the detector in a plane transverse to the direction of the incident particle. This specifies the sampling ratio $R = A_d/A_{sr}$, and the *resampled weight* $w_r = wR$, which is then used as the parameter of a Poisson distribution (w is the weight of the incident particle). From that distribution, one samples the number of particles with that particular energy and direction reaching the detector.

Many studies searching thinning-induced bias can be found in the literature. In Figure 15 the RMS deviations for the ratio of signal density at 600 m from shower axis $S(600)$, the muon density at 1000 m from shower axis $\rho_\mu(1000)$ (observables sensible to

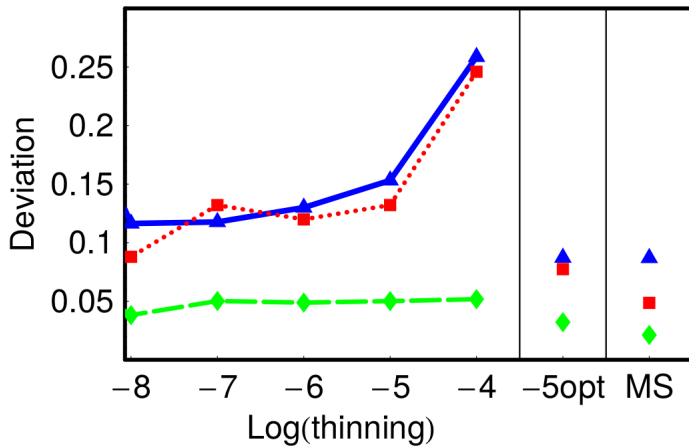


Figure 15 – RMS deviations from unity of $S(600)/S(600)_{\text{no thinning}}$ (blue symbols), $\rho_\mu(1000)/\rho_\mu(1000)_{\text{no thinning}}$ (red symbols) and $X_{\max}/X_{\max, \text{no thinning}}$ (green symbols). The “no thinning” subscript denotes quantities reconstructed for a 10^{18} eV proton shower with no applied thinning, while the other quantities are average reconstructions from sets of simulated showers with the various thinning levels. “Opt -5” denotes thinning factor 10^{-5} with weight limitations and MS denotes multisampling (see (105) for additional details).

Source: GORBUNOV (105)

the primary particle energy (110) and composition (111), respectively) and the X_{\max} and corresponding unthinned quantities, for various thinning factors are shown. Deviations are small, and get negligible when optimal thinning of 10^{-5} with weight limitation is employed, a result consistent with another study analyzing the thinning effect on X_{\max} . (112) The effects of thinning on the signal density and risetime were investigated in (113) by parallelization of the CORSIKA software. Again, deviations were found to be negligible or smaller than detector-to-detector fluctuations.

2.5 Extensive Air Showers Detection

There are several techniques designed to measured EAS observables. The last generation experiments - The Pierre Auger Observatory in the Southern hemisphere and the Telescope Array in the Northern hemisphere - prefer hybrid detection methods, employing fluorescence telescopes detectors and ground arrays. (114, 115)

Fluorescence detectors are employed to study the longitudinal development of the shower: as charged particles propagate through the atmosphere, they excite nitrogen molecules, which then decay to the ground state emitting light. This fluorescent light can be detected by telescopes. Lateral profiles can be reconstructed from ground detectors data. These detectors register mainly electrons, muons and photons that cross them.

2.5.1 Ground detectors

Ground detectors are the most common technique to detect EAS, mostly due to its low cost, wide energy range applicability (they can be used for all energies $E > 10^{14}$ eV), full duty cycle and the ability to easily reconstruct important information about the shower. The lateral distribution slope, arrival time, and curvature of the shower front, as well as geometric reconstruction of the incidence direction of the shower can be accomplished by analysis using multiple data from a grid of detectors at the ground. The area of this array of detectors and the spacing between them depends on the energy range of interest. Common types of ground detectors are the water Cherenkov tanks and scintillators.

Particles propagating through a medium faster than the speed of light in that medium emit radiation, an effect known as the Cherenkov radiation. Cherenkov detectors are tanks filled with pure water and photomultipliers (PMTs), which capture Cherenkov photons generated by superluminal particles. The characteristics of a muon signal and an electron signal are different, a feature that is exploited for detecting the particle type. Thanks to their large dimensions, the detectors are usually sensitive to a broad range of zenith angles, making them good tools to detect inclined air showers.

Scintillators are layers of material which are sensitive to the passage of charged particles. The signal is then amplified by photomultipliers. They are usually small, having areas of a few m^2 , and have thickness of a few centimeters. Consequently, they are sensitive to showers with smaller zenith angles.

Muons have a much greater penetration power than EM particles, so muon detectors can be constructed by shielding common ground detectors. The shielding can be made of lead, iron or even concrete, or simply burying the detectors underground.

2.5.2 Atmospheric Fluorescence Detectors

Shower particles propagating through the atmosphere usually do so in superluminal speeds (with respect to the speed of light in that medium), generating Cherenkov radiation. Additionally, electrons and charged particles excite molecules in the atmosphere, which then emit fluorescence radiation when decaying to the ground state. Atmospheric light detectors explore these features to construct shower observables.

While Cherenkov radiation is beamed in a cone, with opening angle given by $\arccos \theta = 1/(\beta n)$, where β is the velocity in units of the speed of light and n is the refraction index of the medium, fluorescence radiation is emitted isotropically. Therefore, the fluorescence technique is suitable for UHE showers, for only in this high energy regime can the signal be discriminated against the night sky background. Under these conditions the light can be detected up to tens of kilometers away from the shower axis. However, since fluorescence telescopes are very sensitive, measurements are only possible in clear,

moonless nights, rendering a small duty cycle when compared to ground detectors.

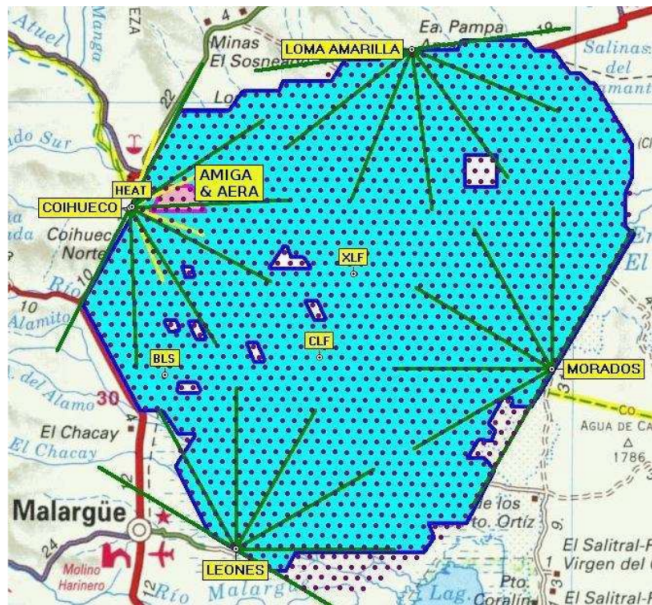


Figure 16 – Pierre Auger Observatory map. The green lines represent the field of view of each one of the 27 telescopes. The names in yellow at the border of the array are the buildings where the telescopes are hosted. XLF and CLF are lasers used for calibration of the fluorescence detectors.

Source: ABRAHAM (114)

2.5.3 The Pierre Auger Observatory

The Pierre Auger Observatory is currently the largest experiment made by mankind. It is a 3000 km^2 array located at Mendoza, Argentina ($35^\circ - 35.5^\circ \text{S}$, $69.0^\circ - 69.6^\circ \text{W}$) at an altitude of 1400 m above sea level. It employs both ground detectors - 1660 units of water Cherenkov tanks in a triangular grid with 1500 m spacing (114–116) - and fluorescence detectors - 27 optical telescopes that overlook the array from 5 different buildings - which record events above 10^{17} eV (117,118) with a duty cycle of about 13%. In Figure 16 a map of the array is displayed.

The Auger Collaboration has contributed in establishing solid evidence for a flux suppression at $4 \times 10^{19} \text{ eV}$ (9,119,120), in setting flux limits for ultra-high energy photons (44,121,122) and neutrinos (123–125) disfavoring top-down models; in establishing a large-scale dipole anisotropy found at energies exceeding the ankle (126), and an unexpected composition evolution in the range from 10^{18} eV to $10^{19.5} \text{ eV}$. (127)

An upgrade for the experiment, the Auger Prime, is in progress. The upgrade will include new 4 m^2 plastic scintillator detectors on top of all Cherenkov detectors, updated and more flexible electronics, a large array of underground muon detectors, and an extended duty cycle for operations of the fluorescence detectors. (128)

2.6 The Muon Production Profile

Since there are still uncertainties regarding cosmic ray composition at ultra-high energy levels, great benefit would result from studying the composition with greater statistics and preferably with other observables than $\langle X_{max} \rangle$ and its RMS.

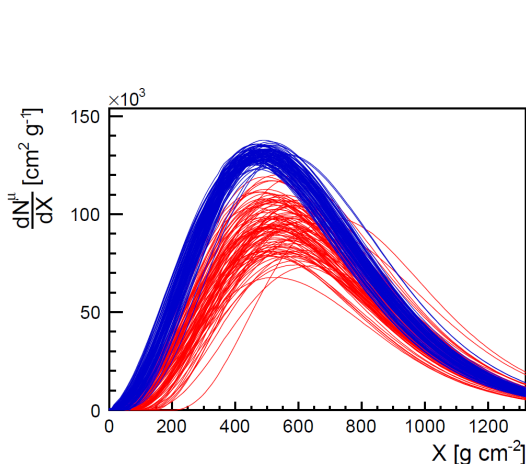


Figure 17 – The muon production profile as simulated for 100 showers for proton (iron) primaries in red (blue) curves.

Source: ANDRINGA (129)

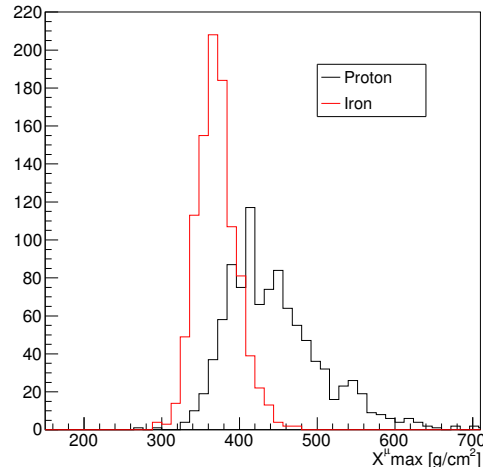


Figure 18 – X_{max}^{μ} distribution for 1000 simulated proton and iron showers using CORSIKA-75000 code. High energy model of choice was QGSJETII04.

Source: By the author.

As has been discussed in section 2.5, the surface detectors are detectors with a full duty cycle, and therefore could improve statistics if an observable exploiting its features could be proposed. Moreover, in section 2.2 we have argued that showers of different hadronic primaries are expected to have different muonic content: heavier primaries should generate showers which are richer in muons.

With this concern in mind, the Auger Collaboration proposed the observable X_{max}^{μ} (130): at each point in the atmosphere along the shower axis, a certain number of muons is produced. The atmospheric depth at which the muons is produced is named the **muon production depth** (MPD). The generation of muons increases up to a point where it reaches a maximum value, and then it mingles. The point at which the production of muons is at its maximum is called the muon production depth at maximum activity, and noted as X_{max}^{μ} . The structure formed by the collection of all MPD is named the **muon production profile**. Figure 17 displays various simulated muons production profiles.

By the superposition principle discussed in section 2.2, a particle of atomic mass A and energy E_0 can be approximated by A proton primaries of energy E_0/A . Two things can then be anticipated: (i) since the shower for heavy primaries develops faster and reaches the critical energy in less generations, X_{max}^{μ} is expected to be shallower when

compared to a proton shower of the same energy; and (ii) since cosmic ray nuclei have higher cross sections, they tend to be less sensitive to fluctuations in the first interaction, so one would expect the RMS of the X_{max}^μ for a heavy primary to be smaller than for a proton primary. Figure 18 shows simulation results of X_{max}^μ for 1000 showers for proton and iron primaries, confirming our expectations.

Since muons travel with little scattering they retain a memory of their production point, an information that can be accessed by measuring its time of arrival. In Figure 19 this process is shown schematically. A muon is produced at a point z along the shower axis, from where it travels a distance ℓ in a straight line with speed c reaching the ground at position (r, ζ) at a normal distance Δ from the shower front plane. Referencing the muon time of flight to the arrival time of the shower-front plane for each position (r, ζ) , we obtain what is defined as the *geometric delay* t_g , which represents the time delay with respect to the shower plane due to a deviation of propagation with respect to the shower axis. Given t_g , it is possible to derive the production distance z of muons for each position (r, ζ) at the ground.

Additional corrections are necessary: muons lose energy in inelastic collisions with atomic electrons, meaning that they travel at speeds smaller than the speed of light ($v_\mu < c$), they scatter elastically when colliding with other nuclei; the geomagnetic field scatters them introducing further delay, and since muons are not produced at the shower axis, an additional correction is necessary to account for the parent meson path. The resulting expression that relates time of arrival with the depth of the production point can be calculated (130–132):

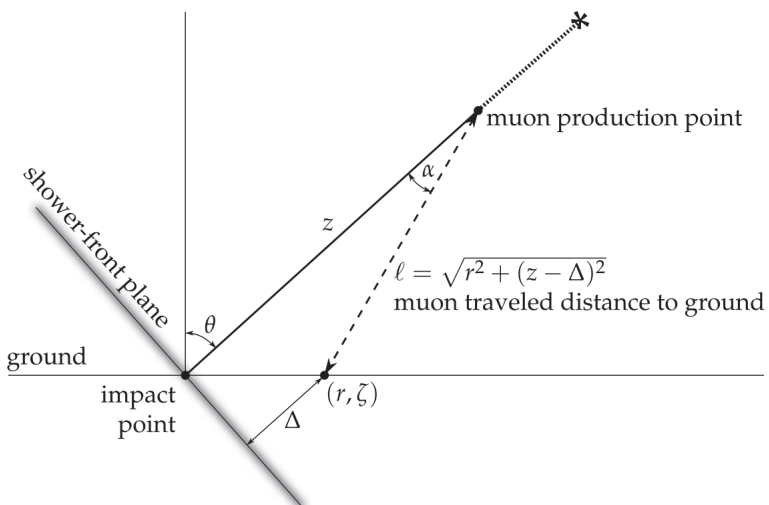


Figure 19 – Geometry used to obtain the muon traveled distance and time delay.
Source: AAB (130)

$$z \approx \frac{1}{2} \left(\frac{r^2}{c(t - \langle t_\varepsilon \rangle)} - c(t - \langle t_\varepsilon \rangle) \right) + \Delta - \langle z_\pi \rangle, \quad (2.17)$$

where $\langle t_\varepsilon \rangle$ is the average time delay due to inelastic scattering with atomic electrons, $\langle z_\pi \rangle$ is the average decay length of a pion and the geometric time delay has been approximated to $t_g \approx t - \langle t_\varepsilon \rangle$. Since this expression accounts for propagation effects, the MPD profile reconstructed with it is called the *apparent* MPD, as opposed to the *total/true* MPD, which accounts for all muons produced irrespective of their chance to reach the ground and be detected.

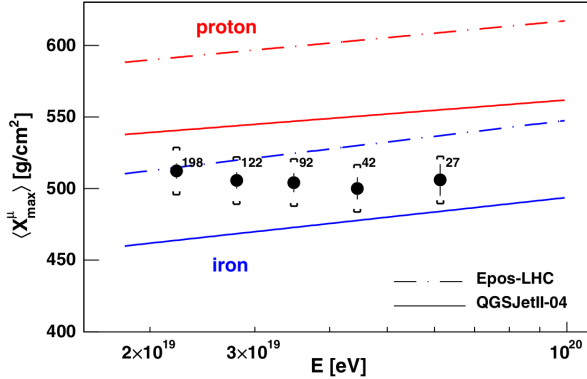


Figure 20 – Evolution with energy of $\langle X_{max}^\mu \rangle$ as measured by the Auger Collaboration (black dots) and predictions from shower simulations using QGSJETII-04 (solid lines) and EPOS-LHC (dotted lines), for a pure proton (iron) composition in red (blue).
Source: AAB (130)

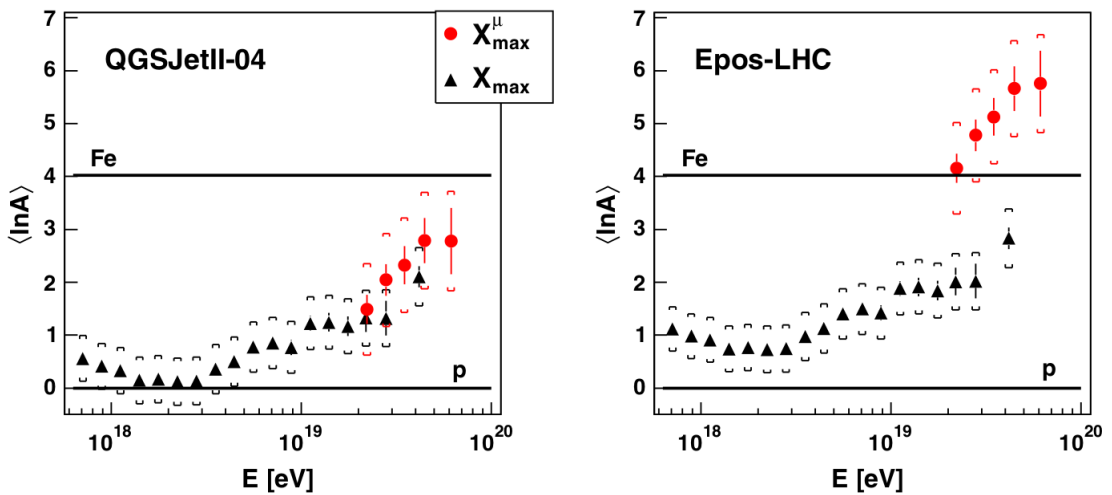


Figure 21 – X_{max} and X_{max}^μ data converted to the mean logarithmic mass, $\langle \ln A \rangle$, compared to QGSJETII-04 (a) and EPOS-LHC (b) predictions.
Source: AAB (130)

Data from about 500 events measured by the Auger Collaboration are displayed in Figure 20. Shown is the evolution of $\langle X_{max}^\mu \rangle$ with energy, as measured by the Collaboration and as it is expected for pure proton or iron composition according to QGSJETII-04 and EPOS-LHC hadronic interaction models. While the data are bracketed by QGSJETII-04 and seem to corroborate the transition to heavier composition interpretation, they are not

bracketed by EPOS-LHC predictions. If interpreted in terms of the latter interaction model, cosmic rays at UHE levels would be heavier than iron primaries.

Since X_{max}^μ and X_{max} are largely correlated by means of the depth of the first interaction (130), the former can be converted to the mean logarithmic mass using similar methods employed for the latter. (133) In Figure 21 the result of this conversion is shown for both X_{max} and X_{max}^μ data. The conclusions are similar: when the data are interpreted with QGSJETII-04, they display a trend to a heavy composition; the same trend for a heavier composition is found when using EPOS-LHC for interpretation, but with an absolute scale shift so that data are not bracketed in the proton-iron predictions. This shows that muon production profile analyses can not only enlighten composition questions, but may select competing high energy interaction hadronic models.

3 THINNING EFFECTS IN THE MUON PRODUCTION PROFILE

In this dissertation we investigate the effects of thinning in the muon production profile simulation. Since we study the effects over all muons generated in the simulation, regardless whether they hit the ground or not, the object of study is the *total/true* muon production profile, and therefore care is needed in interpreting the results.

Section 3.1 clarifies the main differences between what is the object of our study and the observable analyzed in other studies. In section 3.2 we present our investigation into showers simulated with **CORSIKA**. We build a toy Monte Carlo model which mimics some features of an EAS, but more importantly, with which we have full control of a thinning implementation. In order to build the model, some parameterizations were made, and they are presented and discussed in section 3.3. The results of the model and an additional discussion conclude the chapter in section 3.4.

3.1 Differences from the Pierre Auger Collaboration Analysis

The Pierre Auger Collaboration has elaborated a sophisticated data analysis to extract from the measured air shower the relevant information about the muon profile. References (130, 134) summarize the data analysis procedure. The data analysis starts with the arrival times of the particles in the SD stations. A detailed selection procedure was applied in order to minimize systematic and statistical uncertainties, maximize the signal-to-noise ratio and deconvolve detector limitations. Only stations far from the shower axis ($r > 1700$ m) are used and only events with zenith angle lying in the interval $[55^\circ, 65^\circ]$ and energy between $\log(E/\text{eV}) = 19.3 - 20$ are considered.

The arrival time of particles is converted into a muon production depth using a model described in references (131, 132, 135). Note that by this procedure, only muons arriving at the ground contribute to the measured muon profile, therefore low energy muons which might decay during the shower development are not taken into account. A Gaisser-Hillas function is fitted to the longitudinal muon production depth and X_{max}^μ is determined. Finally, in an internal publication* the Pierre Auger Collaboration has evaluated the effect of thinning factors on the muon production depth analysis and has shown to be negligible when thinning levels below 10^{-6} are reached.

The summary of the data analysis of the Pierre Auger Collaboration presented above clarifies the difference between the studies presented here and the detailed analysis done by the Collaboration. We call the main quantity studied here $X_{max}^{\mu-sim}$ to make it

* The Pierre Auger Observatory **Gap Note 2015-34**. Available for collaboration members at: <<https://www.auger.org/index.php/document-centre/viewdownload/114-gap-notes-2015/2351-gap2015-034>>

explicit that we take all muons produced in the simulation (sim) irrespectively of its distance from the shower core. Our study also considers all muons produced in the shower independently if they would hit the ground or not. Moreover we made our study for one fixed energy 10^{18} eV and zenith angle 65° .

Finally, we would like to make it clear that the quantity calculated here $X_{max}^{\mu-sim}$ can not be directly compared to the quantity used by the Pierre Auger Collaboration in its publications and therefore the conclusion can not be extrapolated.

3.2 Effects on CORSIKA profiles

To investigate thinning effects in the muon production profile, many simulations were performed. The software used was CORSIKA-75000.(108) For the high energy model,

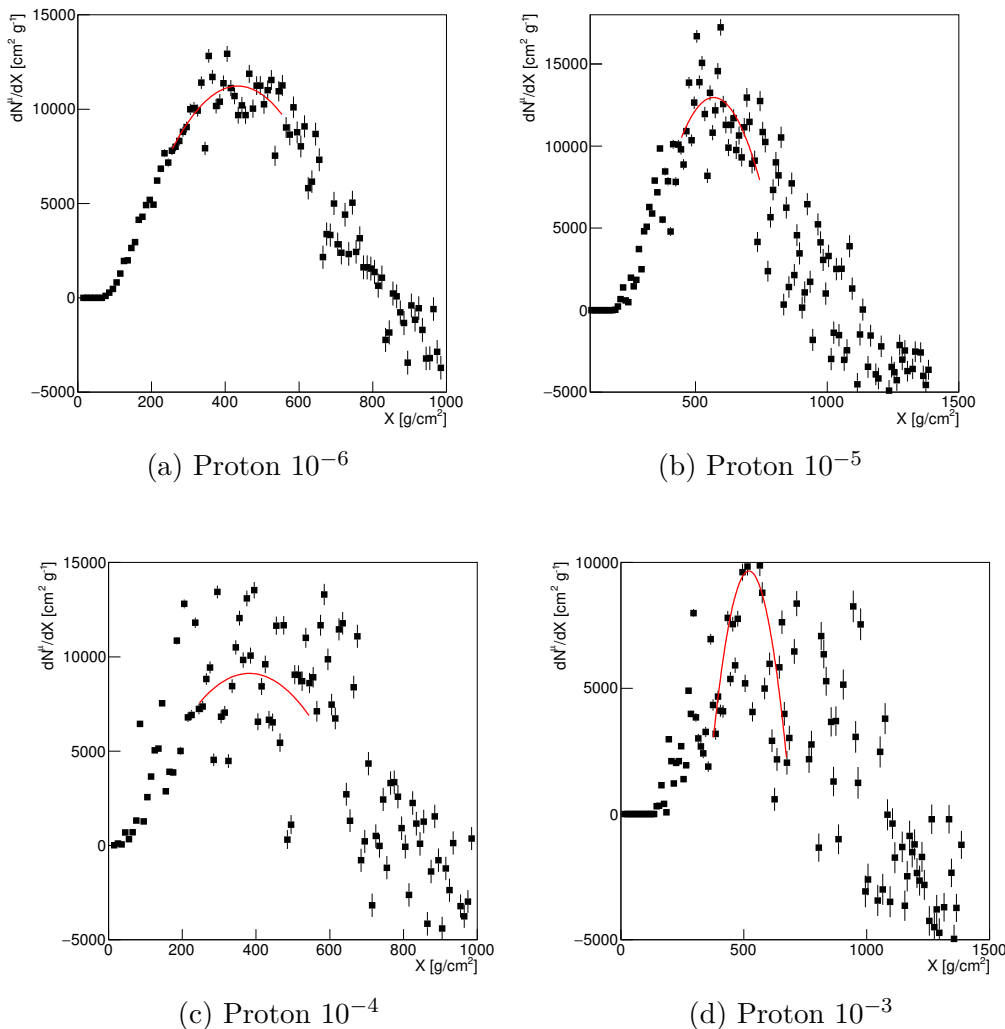


Figure 22 – Muon production profiles simulated with CORSIKA, for a maximum weight of 10^4 and proton primaries. The red line represents a second order polynomial fit used to extract the position of $X_{max}^{\mu-sim}$ (see text)
Source: By the author.

we selected QGSJETII-04 (82) as it has better overall consistency when interpreted in terms of composition with other air shower measurements, such as the X_{max} . The low energy model was set as UrQMD 1.3cr. (89) Energy was fixed as 10^{18} eV and zenith angle as 65° , while the primary particle type was varied. Hadronic and electromagnetic thinning and maximum weight parameters were set to be the same.

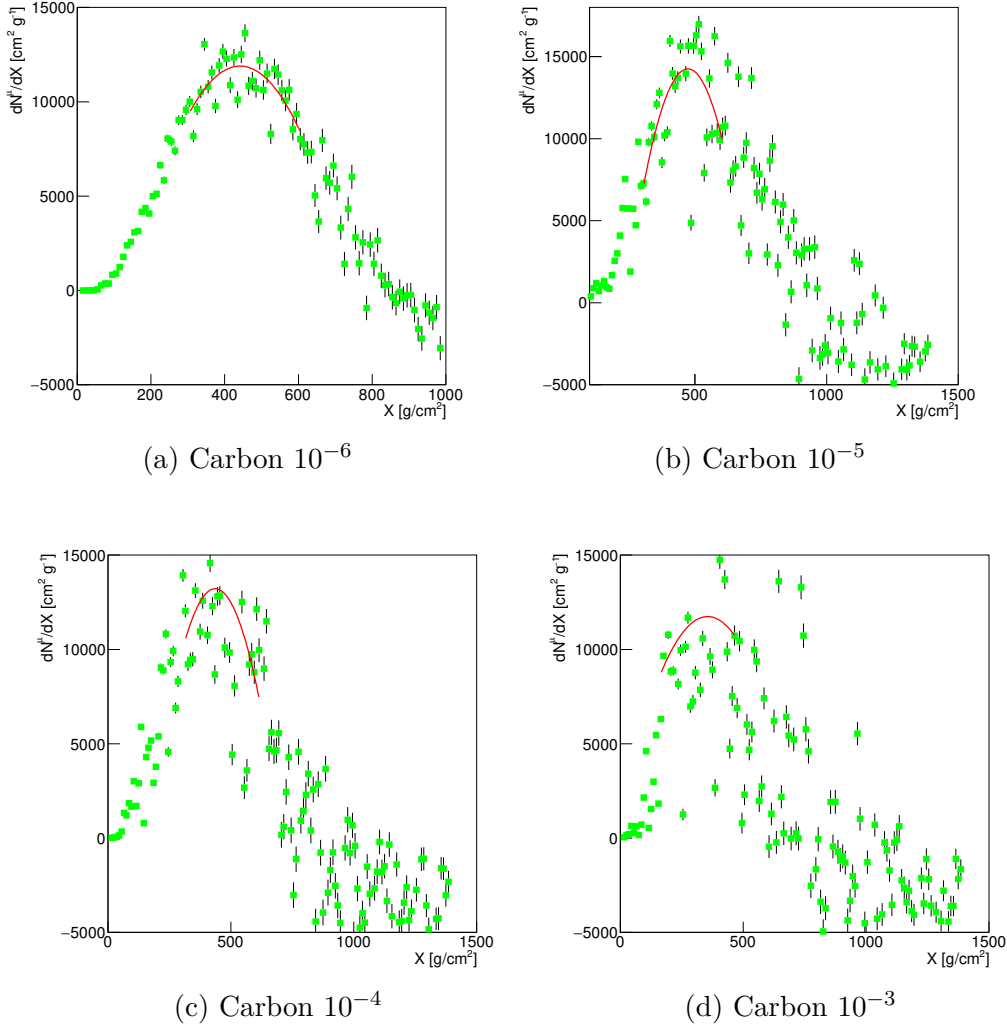


Figure 23 – Muon production profiles simulated with **CORSIKA**, for a maximum weight of 10^4 and carbon primaries. The red line represents a second order polynomial fit used to extract the position of $X_{max}^{\mu-sim}$ (see text)

Source: By the author.

The **CORSIKA** program outputs a file where the number of muons at a given atmospheric depths are provided. This information is displayed in steps of 5 g/cm^2 along the shower axis. We construct a profile by taking the middle point between two successive layers as the abscissa and the difference between the number of muons divided by 5 g/cm^2 as the ordinate. Error bars were calculated by assuming the possibility of Poissonian fluctuations in each bin, thus being equal to the square root of the number of muons at

that given abscissa.

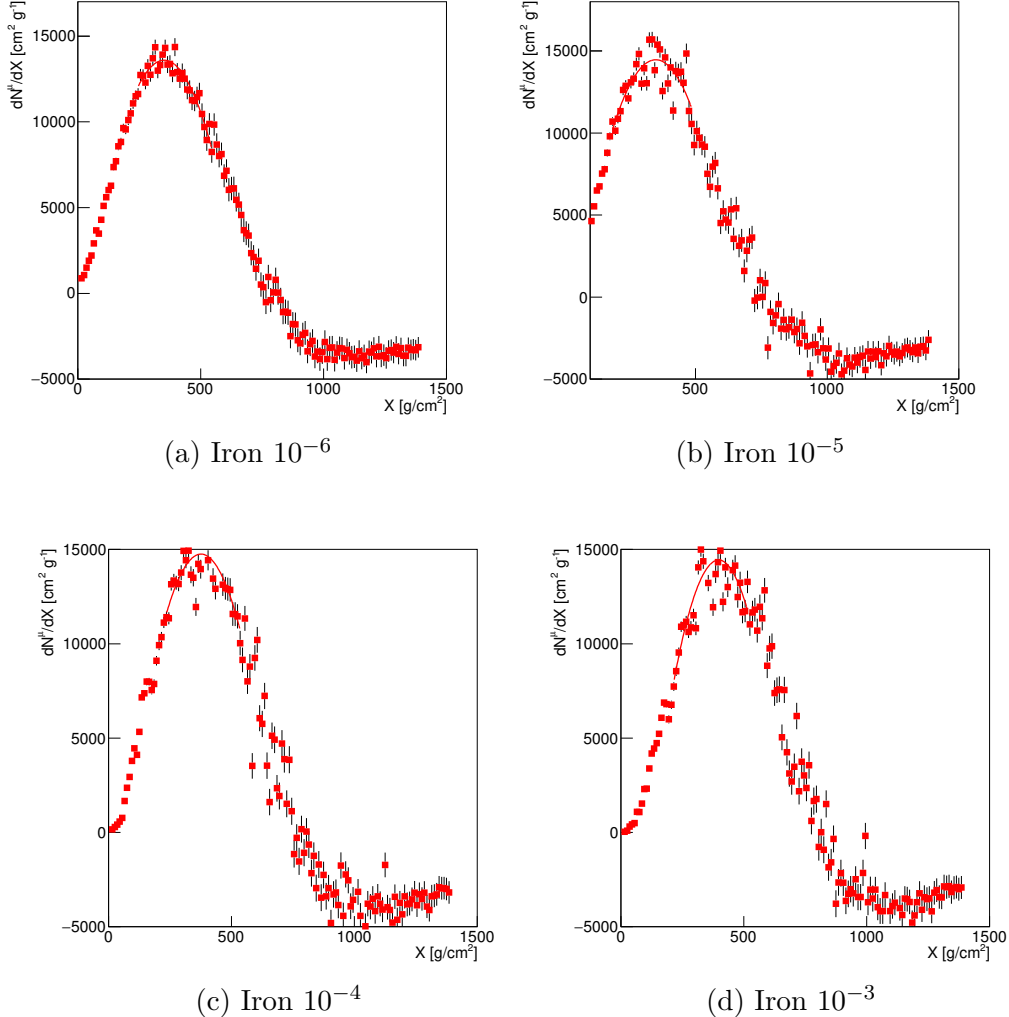


Figure 24 – Muon production profiles simulated with **CORSIKA**, for a maximum weight of 10^4 and iron primaries. The red line represents a second order polynomial fit used to extract the position of $X_{max}^{\mu-sim}$ (see text)

Source: By the author.

For thinning factors 10^{-3} , 10^{-4} , 10^{-5} and 10^{-6} and for each primary particle type, a thousand showers were simulated. The resulting $X_{max}^{\mu-sim}$ was extracted by fitting a second order polynomial function around the nominal maximum. For proton primaries, the procedure was also done varying the maximum weight: maximum values of 10^3 , 10^4 and 10^5 were used. However, we found that the thinning technique may disorganize the profile significantly so as to render it illegible, in a way that the $X_{max}^{\mu-sim}$ position can no longer be reliably obtained by the method described above. In Figure 22, 23, 24 and 25 we display sample profiles for proton, carbon, iron and photon showers, respectively, for all thinning factors. As can be seen, depending on the primary particle, thinning quickly deteriorates the profile: photons are the worst case, where even thinning factors as low as 10^{-5} severely distort the profile, and so no analysis is possible; protons are better behaved,

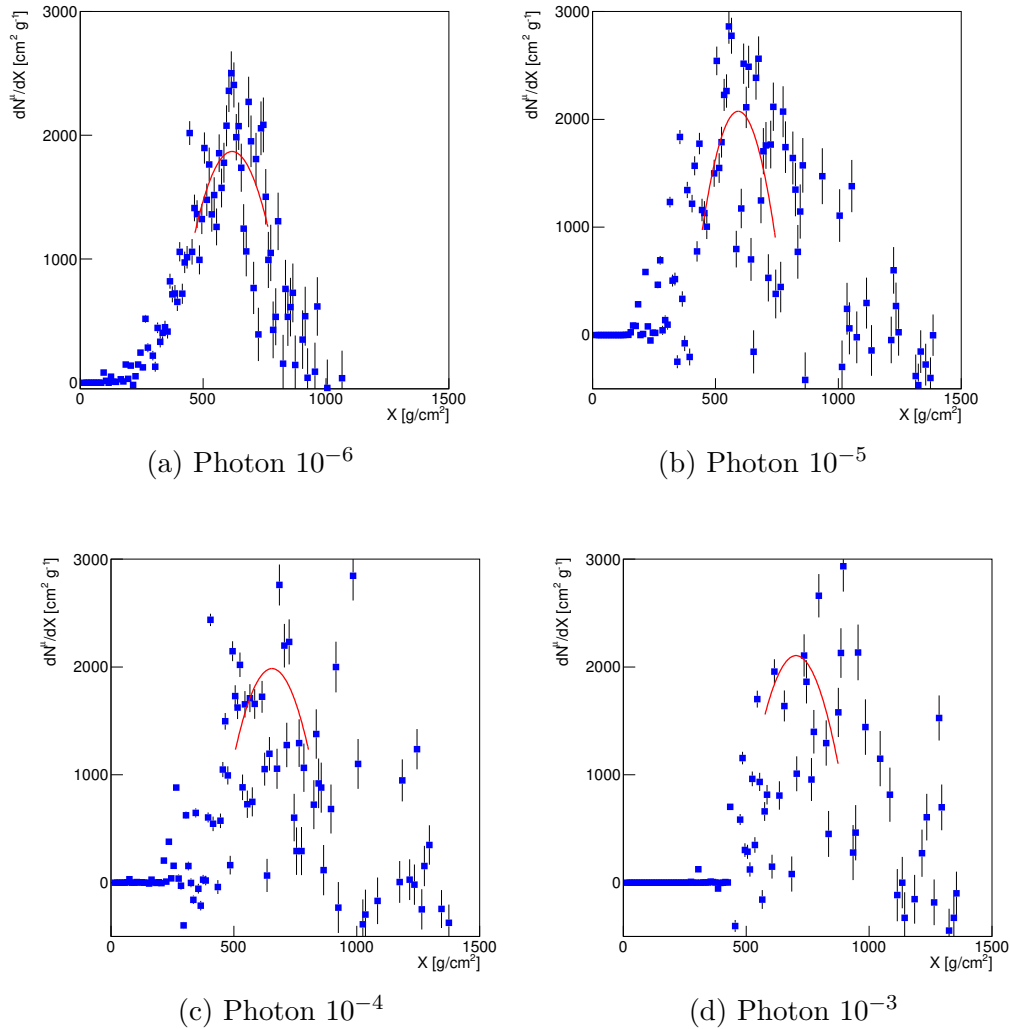


Figure 25 – Muon production profiles simulated with CORSIKA, for a maximum weight of 10^4 and photon primaries. The red line represents a second order polynomial fit used to extract the position of $X_{max}^{\mu-sim}$ (see text)

rendering well-defined profiles up to thinning factors of 10^{-5} , but not for 10^{-4} . Carbon and iron are well behaved: the former can be analyzed up to a thinning factor of 10^{-4} , and the latter up to 10^{-3} . This is due to the absolute number of muons: the distortion is more severe for showers that are poor in muons.

In Figure 26 (a) we display the mean value of $X_{max}^{\mu-sim}$ for 1000 simulated proton showers, for each thinning factor and varying maximum weight limitation. For maximum weight of 10000 and 100000, it appears that deeper profiles are produced, in average, a trend not confirmed when the maximum weight of 1000 is analyzed. While it might be possible that thinning induces effects in the profile, current statistics cannot discriminate a trend.

Figure 26 (b) displays the result for average $X_{max}^{\mu-sim}$ for thinning factors up to 10^{-4}

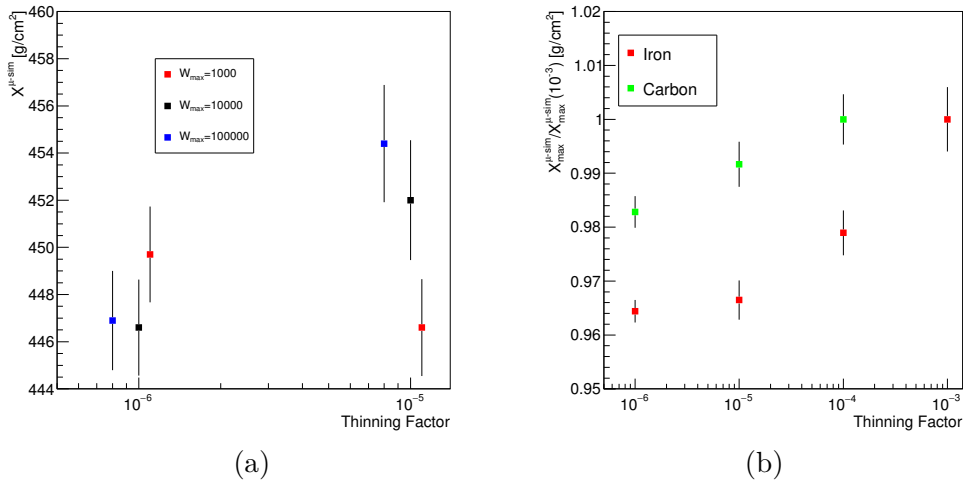


Figure 26 – $X_{max}^{\mu-sim}$ as a function of thinning factor for proton simulated showers (a) and iron and carbon simulated showers (b). Values in (b) are normalized by $X_{max}^{\mu-sim}$ at the maximum thinning factor admitted for that particular primary (10^{-3} for iron, 10^{-4} for carbon). Maximum weight was set to 10000, both for electromagnetic and hadronic particles. Points in (a) were artificially displaced along the horizontal axis so that the error bars do not overlap.

Source: By the author.

for carbon and up to 10^{-3} for iron, normalized by the $X_{max}^{\mu-sim}$ value at thinning 10^{-3} for iron and 10^{-4} for carbon. This is done because the absolute scales of $X_{max}^{\mu-sim}$ are different for carbon and iron, and may conceal the shifts that were found. A trend is suggested: as the thinning factor approaches unit, profiles get deeper, in average. This behavior is verified both for carbon and iron primaries.

Since photon showers do not render legible profiles even for thinning factors as low as 10^{-5} , it is not possible to draw any conclusions about their $X_{max}^{\mu-sim}$ behavior.

3.3 Parameterization

Further insights about the effect of thinning on the muon production profile simulation could be achieved if we modify the thinning algorithm and look for responses generated by the profile. Since **CORSIKA** is a very complex code that implements many effects that might not be related to the muon production profile, a code written only for the profile study would keep the analysis simpler and make any effects more salient. The results of this code cannot, naturally, be compared to full simulations. Its only purpose is a self-consistent analysis.

A proper code for studying thinning effects in the muon production profile must have the following features:

- A reasonable simulation of the hadronic component of the shower. Since muons are

generated mainly by pion decays, at least the multiplicity and energy distribution of pions in a given interaction of a particle with an air nucleus should be mimicked;

- Since the resulting particles of the first interaction strongly affect the shower development, a good representation of the number and energy of pions in the first interaction is important;
- Implementation of the decay and interaction algorithm used in **CORSIKA**, since it is expected that any effect in the muon production profile due to thinning implementations should be caused by a change in the number of produced muons;
- Full control over thinning implementation, with an initial implementation equal to the one used in **CORSIKA**.

With these points in mind, we constructed a code that implemented only the hadronic component of an air shower, simulating only charged pions.

For the first interaction, we used only proton primaries. We constructed frequency histograms for the pion multiplicity and energy distribution in proton-air collisions. Subsequently, we parameterized the multiplicity and the number of generated pions in pion-air collisions.

For proton-air collisions (specifically, proton-nitrogen collision), and energies 10^{16} , 10^{17} , 10^{18} , 10^{19} and 10^{20} eV a hundred thousand collisions were simulated for each energy, using the **CRMC** code (136), and using **QGSJETII-04** (82) as the high energy hadronic interaction model. The program outputs all particles that are generated and their respective energy. With these data, we build a pion multiplicity histogram: for each event, the number of charged pions is counted. In our code the number of pions generated in the first interaction is then sampled for this histograms, for each energy.

In Figure 27 we show the constructed histograms for three different energies. They are normalized by the total number of events for each energy.

Figure 28 displays the energy distribution of the pions generated in proton-nitrogen interaction, as simulated by **CRMC**. For each collision, the logarithm of the energy of each pion was collected. To each entry is also assigned a weight equal to the inverse of the total number of pions generated in that particular collision. This is done in order to cancel artificial fluctuations generated by collisions with few pions, which would disproportionately enhance some regions of the distribution. Thus, when the energy of a pion generated in the first interaction is required, a value is sampled from the distribution corresponding to the primary particle energy.

Sampling directly from histograms is not appropriate for the case of pion-nitrogen interactions, for pion energies are not fixed: they are assigned according to the histograms

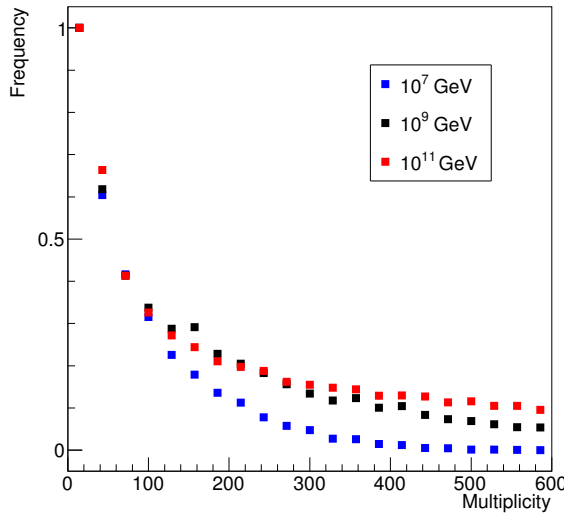


Figure 27 – Charged pion multiplicity in proton-nitrogen collisions as generated by CRMC code for energies 10^7 , 10^9 and 10^{11} GeV.

Source: By the author.

generated in the first interaction, and so there are countless possibilities for their energies. Parameterizations of their multiplicities and energy distribution are required.

For each decade of energy in the range 10^4 up to 8×10^{10} GeV five energies values were chosen and a hundred thousand pion-nitrogen interactions were simulated with CRMC for each value. Multiplicity and energy distribution of charged pions were constructed as in the proton-nitrogen case.

In Figure 29 the multiplicity of pions for a pion-nitrogen collision is shown for 4 different energy values.

We propose an exponential function as a fitting function:

$$\frac{dN}{dM} = N_0 \exp(P_1 M), \quad (3.1)$$

where N_0 is an arbitrary normalization constant and the slope of the exponential, P_1 , is energy dependent. We fit the proposed function to each histogram, and collect the value obtained for the parameter P_1 which best adjusts the function to the data.

In Figure 30 we show the values collected and a power-law parameterization of the energy evolution, A/E^B , with $A = 1.35$ and $B = 0.29$.

The multiplicity function with the slope energy evolution properly parameterized is then fitted to the histograms, and the results can be seen in Figure 29, where the function is displayed as red lines. We did not extend the parameterization to the region $0 \leq M \leq 100$, because we could not find a simple function with few parameters capable of describing the entire multiplicity range, thanks to a protuberant peak close to low M

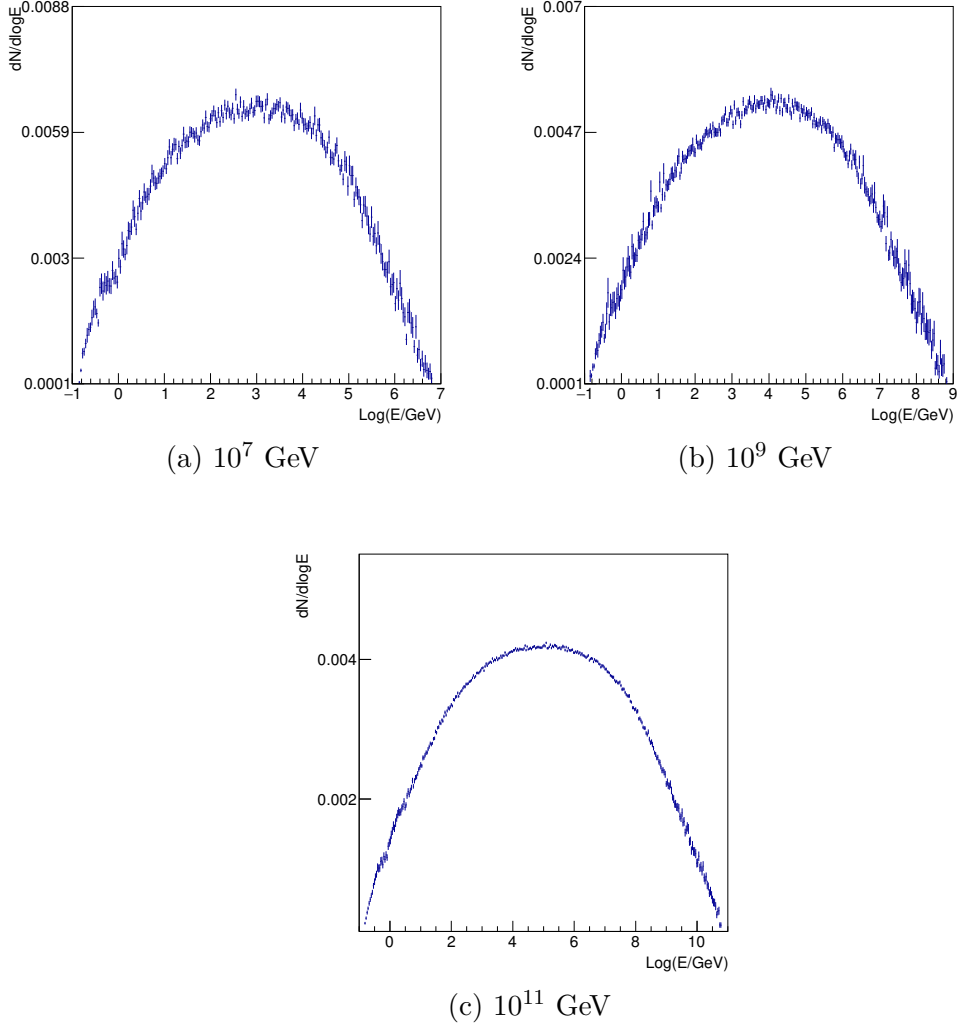


Figure 28 – Energy distribution of pions generated in proton-nitrogen collisions, for energies of 10^7 (a), 10^8 (b) and 10^{11} GeV.

Source: By the author.

values. As a result our parameterization underestimates the frequency of low M . The suppression at the end of the distribution is also not very well described. Nevertheless, at least for intermediate energies the behavior is reasonably well reproduced. While the agreement is certainly not excellent, our only ambition with the parameterization is to use it in a self-consistent toy model study, so that a simple parameterization was preferred, even at risk of inaccuracies, rather than a more complicated although more exact one.

Figure 31 displays the pions energy distribution. We propose a generalized asymmetric gaussian as a fitting function:

$$\frac{dN}{d\log E} = \begin{cases} N_0 \exp \left[-P_2^{\rho/2} |E - P_1|^{\rho} \right], & \text{if } E \leq P_1, \\ N_0 \exp \left[-P_3^{\rho/2} |E - P_1|^{\rho} \right], & \text{if } E > P_1, \end{cases} \quad (3.2)$$

where N_0 is an arbitrary normalization constant, P_1 is the mean (energy dependent)

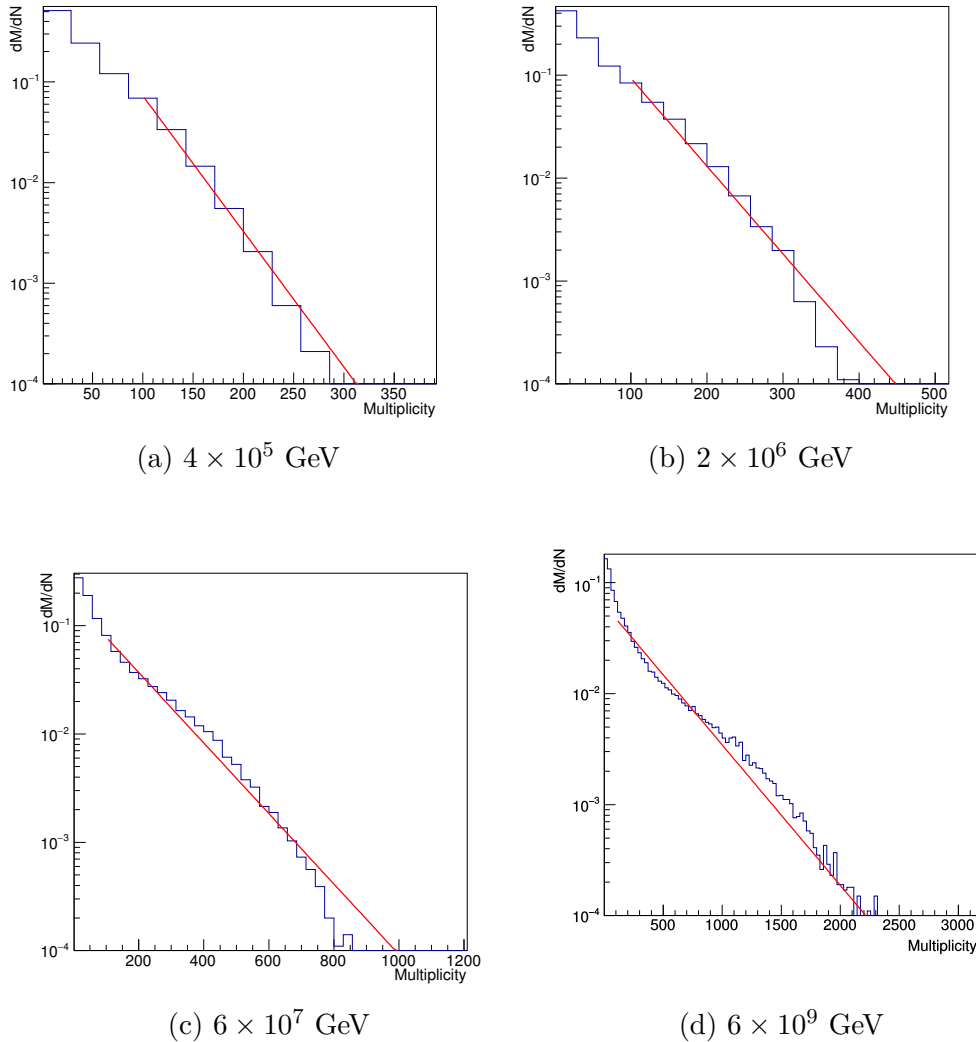


Figure 29 – Multiplicity distributions in pion-nitrogen collisions for energies of 4×10^5 (a), 2×10^6 (b), 6×10^7 (c) and 6×10^9 GeV. The red line is the proposed fit (see text).
Source: By the author.

value, P_2 and P_3 are the asymmetric deviations, which are also energy dependent. The ρ parameter governs the flatness of the gaussian peak. The best value for all energies was found to be $\rho = 3$.

We fit Eq.(3.2) to all energy distributions constructed and extract all optimal values for P_1 . The results are shown in Figure 32 (a), as well as the proposed description of the energy evolution of the parameter: a logarithmic increase in the form $A \log(E) + B$, the best values being $A = 0.232$, $B = -0.685$.

We then fix the parameter P_1 and fit Eq.(3.2) one more time to all constructed distributions. This time, we analyze the behavior of the parameter P_3 , constructing the graph displayed in Figure 32 (b). A power law $AE^B + C$ was proposed as a parameterization, with the best fit values resulting in $A = 0.324$, $B = -0.095$ and $C = 0.020$. The red curve

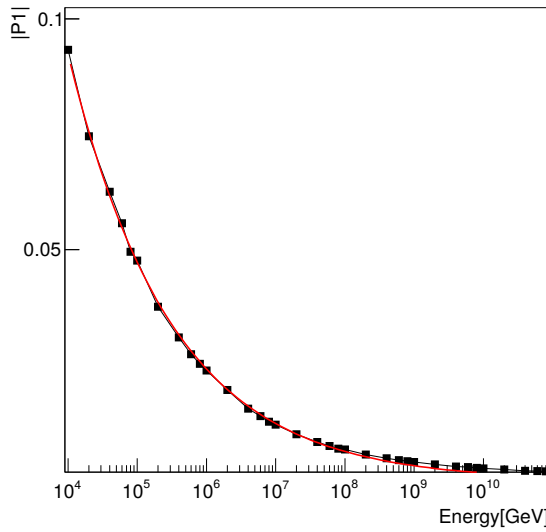


Figure 30 – Evolution with energy of the slope parameter of the exponential function used as parameterization of the multiplicity distribution. In red is a fitted power law function. The fitted function is a power-law $1.35(E/\text{GeV})^{-0.29}$.

Source: By the author.

in Figure 32 (b) shows the resulting fit.

Finally, now with P_1 and P_3 fixed we repeat the procedure for the parameter P_2 : Eq.(3.2) was fitted to the energy distributions, and we construct the graph displayed in Figure 32 (c), were the power law $AE^B + C$ was proposed as the best parameterization, with $A = 0.879$, $B = -0.144$ and $C = 0.013$ being the best values for the constants.

The red curves in Figure 32 show the fit result of Eq.(3.2), with the only free parameter being the normalization constant, N_0 , which is not important since the distributions will have to be normalized in order to perform Monte Carlo calculations. The function describes the behavior of the distribution well, with a few exceptions. At low energies the central plateau is slightly underestimated, as shown in Figure 32 (a), while the tails are problematic both at high and low energy regime.

As was previously mentioned, our goal is a self-consistent comparison of the thinning effect in a toy Monte Carlo model, so the disagreements between the parameterized function and the constructed distributions are not a cause for alarm. The overall qualitative description of the energy distribution and multiplicity is well reproduced in the parameterizations.

3.4 Toy model and discussion

Our model can be described briefly in the following steps:

The first interaction is simulated by randomly generating pions from the multiplicity histograms constructed for proton-nitrogen interactions. In doing so, we restricts ourselves

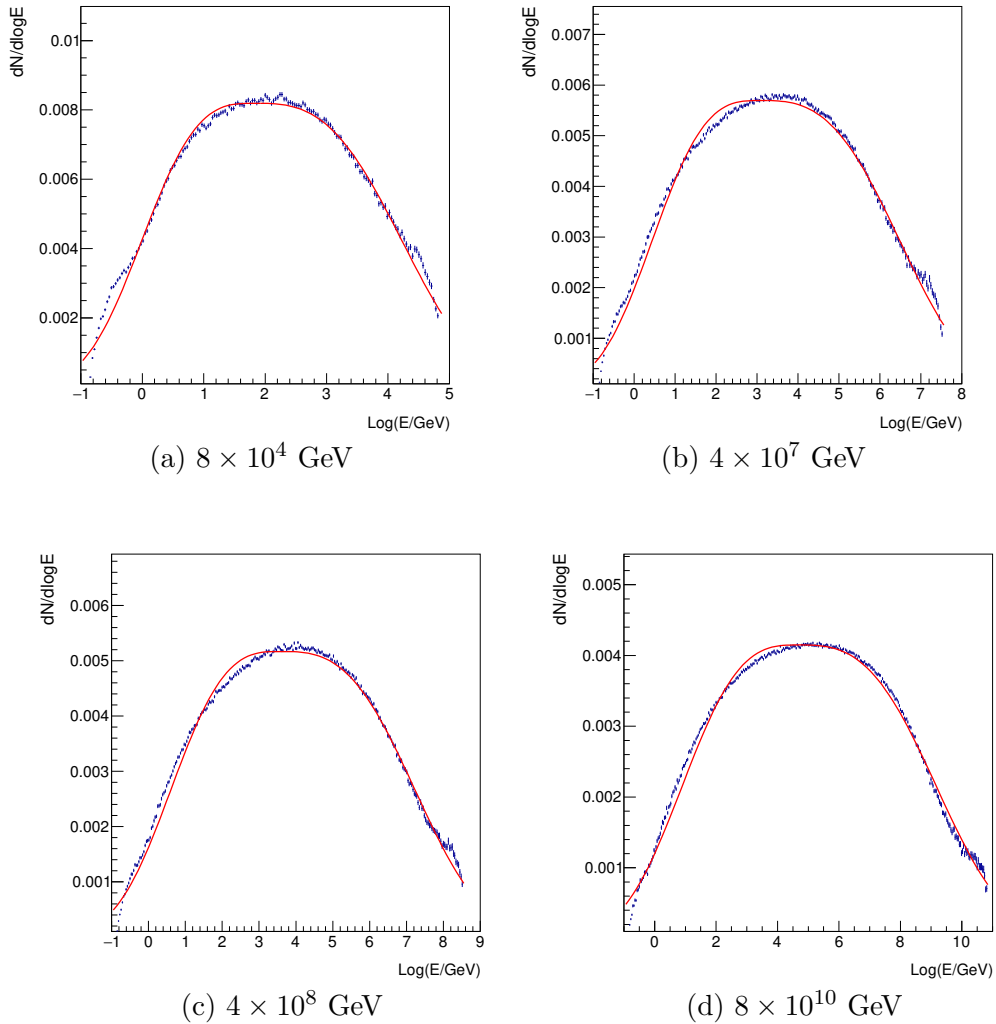


Figure 31 – Energy distribution of generated pions in pion-nitrogen collisions for energies of 8×10^4 (a), 4×10^7 (b), 4×10^8 (c) and 8×10^{10} GeV (d).

Source: By the author.

to simulating primary particles with energies 10^7 , 10^8 , 10^9 , 10^{10} and 10^{11} GeV. For each of these pions, an energy value is sampled from the corresponding energy distributions. If the energy sum of all pions exceeds the primary particle energy, the pion number is halted at the current value and no additional pions are generated. Since in a full shower simulation much of the primary particle energy is transported to the electromagnetic cascade, no action is taken if the sum of all pion energies is beneath the primary particle energy. All generated pions are subject to the thinning algorithm as described in chapter 2.

For each generated pion, a decay length λ_d and an interaction length λ_{int} are generated from probability distributions (details will be discussed later in this section). This determines if a pion will interact or decay: if $\lambda_d < \lambda_{int}$ the pion decays, otherwise it interacts. If the pion will decay, it is relocated to the new position in the atmosphere given by its old position added to λ_d (pions in the first interaction are considered to be

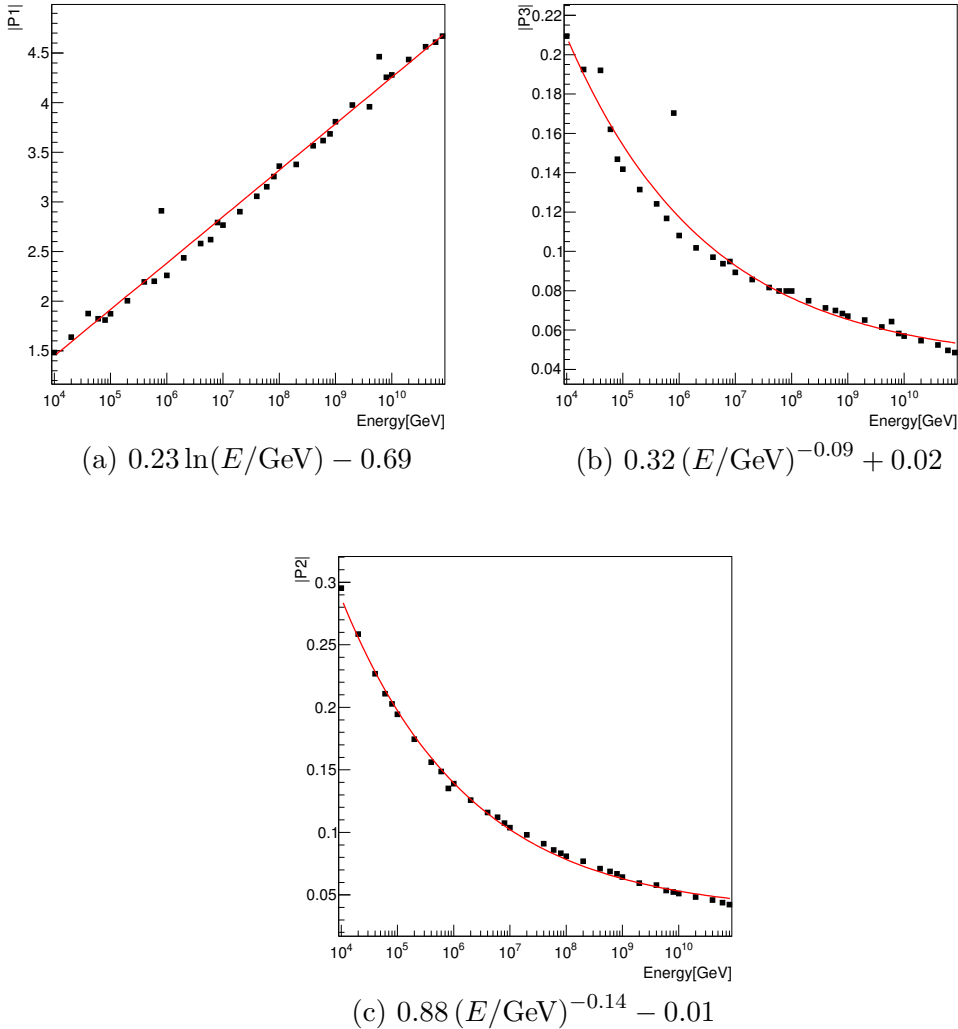


Figure 32 – The energy evolution of the fitting function parameters proposed to describe the pion energy distribution in a pion-nitrogen collision. Red curves are the proposed parameterization of the evolution. P_1 was fitted with all parameters free; P_3 was fitted with P_2 free and P_1 fixed, and P_2 was fitted with P_1 and P_3 fixed.

Source: By the author.

generated at the top of the atmosphere, with $X = 0$). It is then transformed into a muon and not propagated further.

If the pion interacts, it is relocated to the new position in the atmosphere, this time given by its old position added to λ_{int} . Then new pions are generated using the corresponding multiplicity distribution for the parent pion energy, and to each new pion is assigned an energy from the corresponding energy distribution function generated by the parent pion energy. Again, if the energy sum of all generated pions exceed the parent pion energy, pions generation is halted. The generated pions are subject to the thinning process.

The steps of pion generation and decay are repeated until all pions in the simulation decay into muons. When this happens, the simulation is terminated.

The interaction and decay lengths are drawn from the same probabilities distributions employed in **CORSIKA** code (108):

$$P_{int}(\lambda) = \frac{1}{\lambda_{int}} e^{-\lambda/\lambda_{int}}, \quad (3.3)$$

where $\lambda_{int} = m_{air}/\sigma_{int}$ is the mean interaction free path for hadrons in air (in g/cm²), $m_{air} = 14.54$ g/mol is the average atomic weight of air and σ_{int} is the interaction cross-section, which is parameterized from data provided in (108):

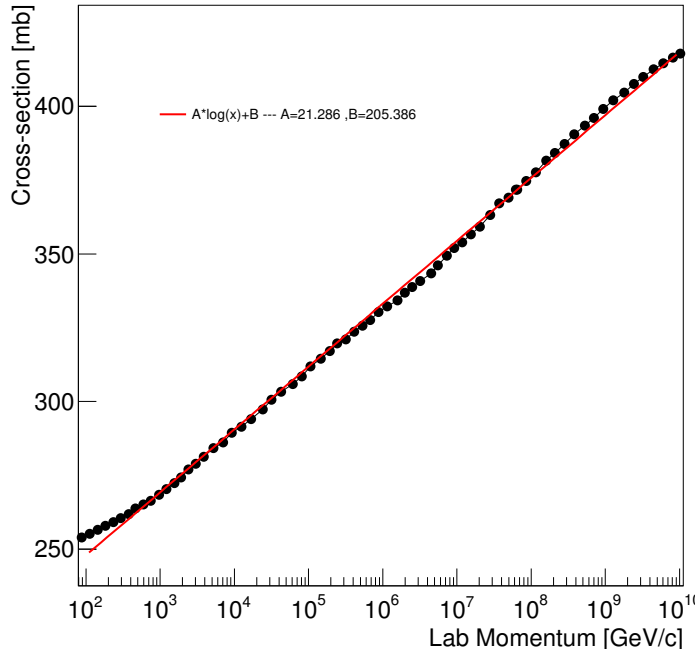


Figure 33 – Hadronic interaction inelastic cross-section as a function of the lab momentum p and corresponding parameterization $A \log(p) + B$, shown as the red curve. Data extracted from (108).

Source: By the author.

$$\sigma_{int}(p) = [21.29 * \log(p/(\text{GeV}/c)) + 205.39] \text{ mb}, \quad (3.4)$$

with p in GeV. This parameterization does not include energies lower than 100 GeV, so our code considers that all particles with $E < 100$ GeV decay into muons at their current position. The decay length is given by:

$$P_D(l) = \frac{1}{l_d} e^{-l/l_d}, \quad (3.5)$$

where $l_d = c\tau_\pi\gamma_\pi\beta_\pi$ is the mean decay length; c is the speed of light, τ_π is the pion life time at rest, γ_π is its Lorentz factor and β_π its velocity in units of the speed of light.

This distribution in length can be converted into a distribution in terms of the atmospheric depth with the use of the mass overburden function $T(h)$. It maps the altitude h in the atmosphere to the corresponding atmospheric depth. To do so, the function divides the atmosphere in four layers, taking a different form or adopting different parameters depending on the layer. In the first layer it can be written as:

$$T(h) = a_5 - b_5 \frac{h}{c_5}, \quad (3.6)$$

where a_5, b_5 and c_5 are constants. In the other four layers the mass overburden is given by:

$$T(h) = a_i + b_i e^{-h/c_i}, \quad (3.7)$$

where a_i, b_i and c_i are constants in a same layer. We chose the U.S standard atmosphere as a parameterization of the atmosphere. (108)

A particle at initial position h_0 that is displaced to a position h forming an angle θ with the vertical direction traverses a path

$$\lambda = f(l, h_0, \theta) = \frac{T(h) - T(h_0)}{\cos \theta} \quad (3.8)$$

in g/cm². So, the probability decay distribution as a function of λ can be written as:

$$P_D(\lambda) = P_D(l) \frac{dl}{d\lambda} = P[f^{-1}(\lambda)] \frac{df^{-1}(\lambda)}{d\lambda}, \quad (3.9)$$

where f^{-1} is the inverse of Eq.(3.8).

The code stores the position of every unpropagated muon, which is equivalent to registering their production point. With this information, the muon production profile can be constructed. Figure 34 shows the profile generated for 10⁹ GeV simulated proton showers, with various thinning factors and a second order polynomial fit to extract the value of $X_{max}^{\mu-sim}$. While the profile is well behaved for showers generated without thinning, it can be seen that it quickly becomes undefined as the thinning factor increases.

The peak is not sufficiently well defined so that a second order polynomial fit can be used to find $X_{max}^{\mu-sim}$, even for the reasonable case of 10⁻⁶. In this way, no conclusion can be drawn about the thinning effect over the muon production profile, except that it disturbs greatly the profile shape.

Possible solutions would be to simulate showers with greater energy or with heavier primaries, since the absolute number of muons would then increase and therefore the fluctuations induced by thinning could turn out to be less intense. Alternatively, simulations could be performed with smaller thinning factors, perhaps using 10⁻⁶ as the biggest factor.

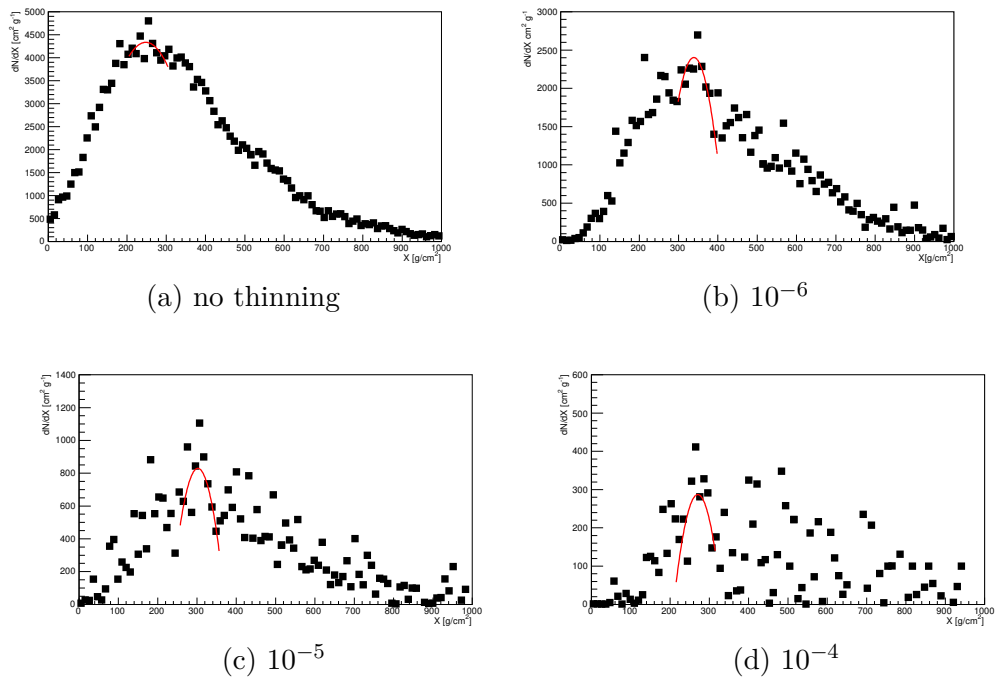


Figure 34 – Muon production profile as generated in the toy model, with thinning factors of 0 (a), 10^{-6} (b), 10^{-5} (c) and 10^{-4} (d). The red curves are second order polynomial fits used to extract $X_{max}^{\mu-sim}$. Profiles were generated for a 10^9 GeV proton at a 65° zenith angle.

Source: By the author.

4 CONCLUSIONS

In light of the persistent competition between different astrophysical scenarios explaining the origin and acceleration of high energy cosmic rays, a solid understanding of the composition behavior in the UHE is paramount.

For a better discrimination, new shower observables (such as the risetime and the muon production depth at maximum activity) were proposed and investigated by the Auger Collaboration. Such observables try to exploit data from surface detectors, which can operate in a full duty cycle and therefore provide a more robust statistical basis for composition analysis.

When the muon production profile measurements are interpreted in terms of the hadronic interaction model QGSJETII-04 (82) the trend is consistent with what was concluded from analysing other observables: it seems that a transition towards heavier elements takes place at ultra-high energies. However, if interpreted in terms of the competing model, EPOS-LHC (81), data would suggest that the composition at UHE is heavier than a pure iron composition. This disagreement should be interpreted with great parcimony, since high energy interaction models are the largest source of uncertainties in extensive air shower simulations.

The thinning technique is an algorithm created for reducing computing time and storage requirements in air shower simulations. While tailored to statistically preserve mean shower quantities of interest, the risk of inducing biases cannot be ruled out without additional investigations. In the literature, attention has been devoted to studying the effects of thinning on the X_{max} , $S(1000)$, $\rho(600)$ and the risetime. (105) (112)-(113) This studies concluded that thinning effects are either negligible or smaller than fluctuations induced by detectors.

In this work we attempted to assess whether the thinning technique induces biases in the total/true muon production profile. Shower simulations were performed with the CORSIKA code (108), reconstructing the muon production profile by extracting the number of muons produced at a given atmospheric depth, for various primary particles with energies of 10^9 GeV and zenith angle of 65° . Our study was inconclusive for proton and photon primaries, because thinning induced fluctuations were so large that they greatly disfigured the muon production profile, making it impossible to accurately determine the $X_{max}^{\mu-sim}$ position. For carbon and iron profiles the fluctuations were less significant, and we found that showers simulated with greater thinning factors tend to produce deeper production profiles.

In the hope of gaining additional insight about the thinning effects over the muon

production profile, we developed a toy Monte Carlo model, implementing just the essential features for the simulation of the hadronic component of an extensive air shower, thus rendering the muon production profile simulation possible. To that end, we simulated a great variety of proton-air and pion-air collisions. Histograms of the pions multiplicities and energy distributions were recorded, and parameterizations were made so that pion-air collisions at arbitrary energies could be simulated. We found that our toy model successfully simulated muon production profiles without thinning. However, thinning introduces artificial fluctuations that were too severe, so that no conclusions could be drawn about its effects over $X_{max}^{\mu-sim}$.

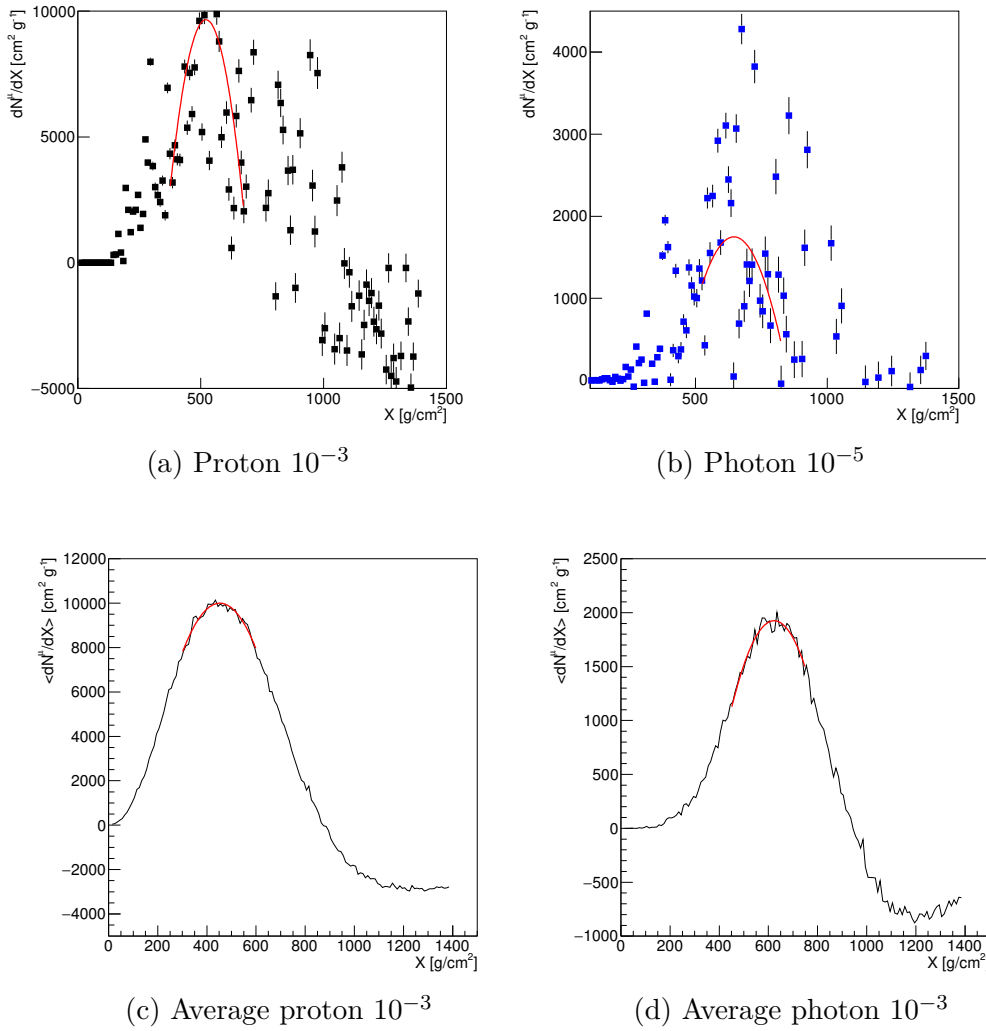


Figure 35 – Sample profiles simulated in an event-to-event basis with **CORSIKA**, (a) and (b) and taking the average of 100 profiles (c) and (d).
Source: By the author.

There are some possibilities to overcome these obstacles in future works. One could simulate profiles with higher primary energies. Since the fluctuations are wider for showers with few muons and the number of muons scales with primary energy, maybe

fluctuations can be kept under control if more energetic showers (perhaps showers of 10^{10} or even 10^{11} GeV) are studied. This is possibly the easiest fix to the problem. By the same reason, simulations with heavier primaries would increase the muonic content of the shower, in this way reducing statistical fluctuations. For that to be possible, however, parameterizations of multiplicity and energy distributions would have to be recalculated for the heavy primaries. A final possibility would be to study the average muon production profile over a series of showers, instead of studying it on an event-to-event basis. In that way, artificial fluctuations would cancel, and a definite profile would be legible.

Figure 35 shows two sample profiles obtained on an event-to-event basis, for a primary proton with a thinning factor of 10^{-3} (a) and primary photon of 10^{-5} (b). As can be seen, the profiles are completely scattered and the positions of their maximum cannot be correctly determined. In Figure 35 (c) and (d) we show profiles constructed taking the average number of muons produced at a given atmospheric depth for 100 simulated showers, for proton and photons primaries with thinning factors of 10^{-3} . It can be seen that now the profiles are well behaved: it is possible to extract the position of $X_{max}^{\mu-sim}$. If this is done, then thinning effects would need to be reevaluated in CORSIKA simulations, and the toy model would still need to be tested for this sort of study.

All in all, it is possible to conclude that thinning does produce discernible effects over the true/total muon production profiles simulations, at least for some primary particles, with an energy of 10^9 GeV and for zenith angles of 65° , using QGSJETII-04 as the high energy interaction model. The causes of the observed effect, as well as its relevance for composition analysis, remain unclear and need further investigation.

REFERENCES

- 1 HESS, V. The highest-energy cosmic rays. **Physikalische Zeitschrift**, v. 13, p. 1084, 1912.
- 2 OLIVE, K.A. et al. Review of particle physics. **Chinese Physics C**, v. 38, n. 9, p. 090001, 2014.
- 3 IVANOV, A. A.; KNURENKO, S. P.; SLEPTSOV, I. Y. Measuring extensive air showers with Cherenkov light detectors of the Yakutsk array: the energy spectrum of cosmic rays. **New Journal of Physics**, v. 11, p. 065008, 2009.
- 4 NAGANO, M. et al. Energy spectrum of primary cosmic rays above 10^{17} eV determined from extensive air shower experiments at Akeno. **Journal of Physics G**, v. 18, n. 2, p. 423, 1992. doi: 10.1088/1367-2630/11/6/065008.
- 5 ANTONI, T. et al. KASCADE measurements of energy spectra for elemental groups of cosmic rays: results and open problems. **Astroparticle Physics**, v. 24, n. 1–2, p. 1, 2005.
- 6 APEL, W. D. et al. Kneelike structure in the spectrum of the heavy component of cosmic rays observed with KASCADE-grande. **Physical Review Letters**, v. 107, n. 17, p. 171104, 2011.
- 7 ABRAHAM, J. et al. Measurement of the energy spectrum of cosmic rays above 10^{18} eV using the Pierre Auger Observatory. **Physics Letters B**, v. 685, n. 4-5, p. 239, 2010.
- 8 BIRD, D.J. et al. Evidence for correlated changes in the spectrum and composition of cosmic rays at extremely high energies. **Physical Review Letters**, v. 71, n. 21, p. 3401, 1993.
- 9 ABRAHAM, J. et al. Observation of the suppression of the flux of cosmic rays above 4×10^{19} eV. **Physical Review Letters**, v. 101, n. 6, p. 61101, 2008.
- 10 ABBASI, R. U. et al. First observation of the Greisen-Zatsepin-Kuzmin suppression. **Physical Review Letters**, v. 100, n. 10, p. 101101, 2008.
- 11 HÖRANDEL, J. R. Models of the knee in the energy spectrum of cosmic rays. **Astroparticle Physics**, v. 21, n. 3, p. 241, 2004.
- 12 STANEV, T.; BIERMANN, P.; GAISSER, T. Cosmic rays. IV. the spectrum and chemical composition above 10^4 GeV. **Astronomy and Astrophysics**, v. 274, n. 3, p. 902, 1993.
- 13 KOBAYAKAWA, K.; HONDA, Y. S.; SAMURA, T. Acceleration by oblique shocks at supernova remnants and cosmic ray spectra around the knee region. **Physical Review D**, v. 66, n. 8, p. 083004, 2002.
- 14 SVESHNIKOVA, L. The knee in the galactic cosmic ray spectrum and variety in supernovae. **Astronomy and Astrophysics**, v. 409, n. 3, p. 799, 2003.

- 15 ERLYKIN, A. D.; WOLFENDALE, A. W. Supernova remnants and the origin of the cosmic radiation: I. SNR acceleration models and their predictions. **Journal of Physics G**, v. 27, n. 5, p. 941, 2001.
- 16 PLAGA, R. A possible universal origin of hadronic cosmic rays from ultrarelativistic ejecta of bipolar supernovae. **New Astronomy**, v. 7, n. 6, p. 317, 2002.
- 17 LAGUTIN, A.; MAKAROV, V.; TYUMENTSEV, A. Anomalous diffusion of the cosmic rays: steady-state solution. **Nuclear Physics B**, v. 97, p. 267, 2001. doi: 10.1016/S0920-5632(01)01282-8.
- 18 CANDIA, J.; MOLLERACH, S.; ROULET, E. Cosmic ray spectrum and anisotropies from the knee to the second knee. **Journal of Cosmology and Astroparticle Physics**, v. 2003, n. 05, p. 003, 2003.
- 19 KARAKULA, S.; TKACZYK, W. The formation of the cosmic ray energy spectrum by a photon field. **Astroparticle Physics**, v. 1, n. 2, p. 229, 1993.
- 20 DOVA, M. T.; EPELE, L. N.; SWAIN, J. D. **Massive relic neutrinos in the galactic halo and the knee in the cosmic ray spectrum**. 2001. Available from: <<http://arxiv.org/abs/astro-ph/0112191>>. Accessible at: 09 Dec.2016.
- 21 CANDIA, J.; EPELE, L. N.; ROULET, E. Cosmic ray photodisintegration and the knee of the spectrum. **Astroparticle Physics**, v. 17, n. 1, p. 23, 2002.
- 22 KAZANAS, D.; NICOLAIDIS, A. **Cosmic ray "knee": a herald of new physics?** 2001. Available from: <<http://arxiv.org/abs/astro-ph/0103147>>. Accessible at: 09 Dec.2016.
- 23 KAZANAS, D; NICOLAIDIS, A. Cosmic rays and large extra dimensions. **General Relativity and Gravitation**, v. 35, n. 6, p. 1117, 2003.
- 24 LINSLEY, J. Primary cosmic rays of energy 10^{17} to 10^{20} ev, the energy spectrum and arrival directions. In: INTERNATIONAL COSMIC RAY CONFERENCE, ICRC, 8th, 1963, Jaipur, India. **Proceedings...**Jaipur: ICRC, 1963. v. 4, p. 77.
- 25 ALLARD, D.; PARIZOT, E.; OLINTO, A. V. On the transition from galactic to extragalactic cosmic-rays: Spectral and composition features from two opposite scenarios. **Astroparticle Physics**, v. 27, n. 1, p. 61, 2007.
- 26 ALOISIO, R.; BEREZINSKY, V.; GAZIZOV, A. Ultra high energy cosmic rays: the disappointing model. **Astroparticle Physics**, v. 34, n. 8, p. 620, 2011.
- 27 BIERMANN, P. L.; SOUZA, V. Centaurus A: the one extragalactic source of cosmic rays with energies above the knee. **The Astrophysical Journal**, v. 746, n. 1, p. 72, 2012.
- 28 HILLAS, A. M. **Cosmic rays:** recent progress and some current questions. 2006. Available in: <<http://arxiv.org/abs/astro-ph/0607109>>. Accessible at: 09 Dec.2016.
- 29 MARCO, D. D.; STANEV, T. On the shape of the ultrahigh energy cosmic ray spectrum. **Physical Review D**, v. 72, n. 8, p. 5, 2005.

- 30 ALOISIO, R.; BEREZINSKY, V.; BLASI, P. Ultra high energy cosmic rays: implications of Auger data for source spectra and chemical composition. **Journal of Cosmology and Astroparticle Physics**, v. 10, p. 20, 2014.
- 31 GIACINTI, G.; KACHELRIESS, M.; SEMIKOZ, D. V. Escape model for Galactic cosmic rays and an early extragalactic transition. **Physical Review D**, v. 91, n. 8, p. 1, 2015.
- 32 GLOBUS, N.; ALLARD, D.; PARIZOT, E. A complete model of the cosmic ray spectrum and composition across the Galactic to extragalactic transition. **Physical Review D**, v. 92, n. 2, p. 021302(R), 2015.
- 33 ALLARD, D.; PARIZOT, E.; KHAN, E.; GORIELY, S.; OLINTO, A. V. UHE nuclei propagation and the interpretation of the ankle in the cosmic-ray spectrum. **Astronomy and Astrophysics**, v. 443, p. L29, 2005. doi: 10.1051/0004-6361:200500199.
- 34 BEREZINSKY, V.; GAZIZOV, A. Z.; GRIGORIEVA, S. I. Dip in UHECR spectrum as signature of proton interaction with CMB. **Physics Letters B**, v. 612, n. 3-4, p. 147, 2005.
- 35 UNGER, M.; FARRAR, G. R.; ANCHORDOQUI, L. A. Origin of the ankle in the ultrahigh energy cosmic ray spectrum, and of the extragalactic protons below it. **Physical Review D**, v. 92, n. 12, p. 123001, 2015.
- 36 GREISEN, K. End to the cosmic-ray spectrum? **Physical Review Letters**, v. 16, n. 17, p. 748, 1966.
- 37 ZATSEPIN, G. T.; KUZMIN, V. A. Upper limit of the spectrum of cosmic rays. **Jetp Letters**, v. 4, n. 3, p. 78, 1966.
- 38 DI MATTEO, A. (on behalf of the Pierre Auger Collaboration). Combined fit of spectrum and composition data as measured by the Pierre Auger Observatory. In: INTERNATIONAL COSMIC RAYS CONFERENCE, ICRC, 34, 2015, The Hague, Netherlands. **Proceedings...**The Hague: ICRC, 2015. p. 14.
- 39 DORMAN, L. I.; VENKATESAN, D. Solar cosmic rays. **Space Science Reviews**, v. 64, n. 3-4, p. 183, 1993.
- 40 ACKERMANN, M. et al. Detection of the characteristic pion-decay signature in supernova remnants. **Science**, v. 339, n. 6121, p. 807, 2013.
- 41 BHATTACHARJEE, P.; HILL, C. T.; SCHRAMM, D. N. Grand unified theories, topological defects, and ultrahigh-energy cosmic rays. **Physical Review Letters**, v. 69, n. 4, p. 567, 1992.
- 42 DREES, M. The top-down interpretation of ultra-high energy cosmic rays. **Journal of the Physical Society of Japan**. v.77, Supl.B, p.16, 2008.
- 43 TORRES, D. F.; ANCHORDOQUI, L. A. Astrophysical origins of ultrahigh energy cosmic rays. **Reports on Progress in Physics**, v. 67, n. 9, p. 1663, 2004.
- 44 ABRAHAM, J. et al. Upper limit on the cosmic-ray photon fraction at EeV energies from the Pierre Auger Observatory. **Astroparticle Physics**, v. 31, n. 6, p. 399, 2009.

- 45 SEMIKOZ, D. V. Constraints on top-down models for the origin of UHECRs from the Pierre Auger Observatory data. In: INTERNATIONAL COSMIC RAYS CONFERENCE, ICRC, 30, 2007, Mérida, Mexico. **Proceedings**...Mérida: ICRC, 2007. p. 30.
- 46 ZAMORANO, B. **Inferring the mass composition of ultra-high-energy cosmic rays through the characterisation of the muon production profile**. 2014. 140 p. Ph.D. Thesis (Physics) — Departamento de Fisica Teorica y del Cosmos & CAFPE, Universidad de Granada, Granada, 2014.
- 47 FERMI, E. On the origin of the cosmic radiation. **Physical Review**, v. 75, n. 8, p. 1169, 1949.
- 48 HILLAS, A. M. The origin of ultra-high-energy cosmic rays. **Annual Review of Astronomy and Astrophysics**, v. 22, n. 1, p. 425, 1984.
- 49 ABRAHAM, J. et al. Correlation of the highest-energy cosmic rays with nearby extragalactic objects. **Science**, v. 318, n. 5852, p. 938, 2007.
- 50 _____. Correlation of the highest-energy cosmic rays with the positions of nearby active galactic nuclei. **Astroparticle Physics**, v. 29, n. 3, p. 188, 2007.
- 51 ABREU, P. et al. Update on the correlation of the highest energy cosmic rays with nearby extragalactic matter. **Astroparticle Physics**, v. 34, n. 5, p. 314, 2010.
- 52 AAB, A. et al. Searches for anisotropies in the arrival directions of the highest energy cosmic rays detected by the Pierre Auger observatory. **The Astrophysical Journal**, v. 804, n. 1, p. 15, 2015.
- 53 BLÜMER, J.; ENGEL, R.; HÖRANDEL, J. R. Cosmic rays from the knee to the highest energies. **Progress in Particle and Nuclear Physics**, v. 63, n. 2, p. 293, 2009.
- 54 MENN, W. et al. The PAMELA space experiment. **Advances in Space Research**, v. 51, n. 2, p. 209, 2013.
- 55 TOMASSETTI, N. AMS-02 in space: physics results. **Journal of Physics: conference series**, v. 650, p. 012001, 2015. doi: 10.1088/1742-6596/650/1/012001.
- 56 LODDERS, K. Solar system abundances and condensation temperatures of the elements. **The Astrophysical Journal**, v. 591, n. 2, p. 1220, 2003.
- 57 ABBASI, R. et al. **Report of the working group on the composition of ultra high energy cosmic rays**. 2015. Available from: <arxiv.org/abs/1503.07540>. Accessible at: 14 Dec.2016.
- 58 ABBASI, R. U. et al. Indications of proton-dominated cosmic-ray composition above 1.6 EeV. **Physical Review Letters**, v. 104, n. 16, p. 1, 2010.
- 59 KNURENKO, S. P.; SABOUROV, A. Study of cosmic rays at the Yakutsk EAS array: energy spectrum and mass composition. **Nuclear Physics B**, v. 212-213, p. 241, 2011. doi: 10.1016/j.nuclphysbps.2011.03.033.
- 60 JUI, C. C. H. Cosmic ray in the northern hemisphere: Results from the telescope array experiment. **Journal of Physics: conference series**, v. 404, n. 1, p. 012037, 2012.

- 61 FACAL SAN LUIS, P. (on behalf of the Pierre Auger Collaboration). The distribution of shower maxima of UHECR air showers. In: INTERNATIONAL COSMIC RAYS CONFERENCE, ICRC, 32, 2011, Beijing, China. **Proceedings**...Beijing: ICRC, 2011. v. 2, p. 105.
- 62 DOVA, M. T.; MANCEÑIDO, M. E.; MARIAZZI, A. G.; WAHLBERG, H.; ARQUEROS, F.; GARCÍA-PINTO, D. Time asymmetries in extensive air showers: a novel method to identify UHECR species. **Astroparticle Physics**, v. 31, n. 4, p. 312, 2009.
- 63 AAB, A. et al. Azimuthal asymmetry in the risetime of the surface detector signals of the Pierre Auger Observatory. **Physical Review D**, v. 93, n. 7, p. 1, 2016.
- 64 AIR shower (physics). 2016. Available from: <[https://en.wikipedia.org/wiki/Air_shower_\(physics\)](https://en.wikipedia.org/wiki/Air_shower_(physics))#/media/File:AirShower.svg>. Accessible at: 08 Dec.2016.
- 65 HEITLER, W. **The quantum theory of radiation**. London: Oxford University Press, 1936.
- 66 NELSON, W.; HIRAYAMA, H.; ROGERS, D. **The EGS4 code system**. Stanford, 1985. Technical report SLAC 265.
- 67 FERRARI, A.; SALA, R.; FASSO, A.; RANFT, J. **FLUKA**: a multi-particle transport code. Stanford, 2005. v. 5. Technical report.
- 68 AGOSTINELLI, S. et al. GEANT4 - a simulation toolkit. **Nuclear Instruments and Methods in Physics Research**:section A, v. 506, n. 3, p. 250, 2003.
- 69 DEDENKO, L. A new method of solving the nuclear cascade equations. In: INTERNATIONAL COSMIC RAYS CONFERENCE, ICRC, 9, 1965, London, United Kingdom. **Proceedings**...London: ICRC, 1965. v. 1, p. 662.
- 70 BOSSARD, G.; DRESCHER, H. J.; KALMYKOV, N. N.; OSTAPCHENKO, S.; PAVLOV, A. I.; PIEROG, T.; VISHNEVSKAYA, E. A.; WERNER, K. Cosmic ray air shower characteristics in the framework of the parton-based Gribov-Regge model NEXUS. **Physical Review D**, v. 63, p. 054030, 2001. doi: 10.1103/PhysRevD.63.054030.
- 71 ALLEN, J. et al. Air shower simulation and hadronic interactions. **EPJ Web of Conferences**, v. 53, p. 01007, 2013. doi: 10.1051/epjconf/20135300001.
- 72 ENGEL, R.; HECK, D.; PIEROG, T. Extensive air showers and hadronic interactions at high energy. **Annual Review of Nuclear and Particle Science**, v. 61, n. 1, p. 467, 2011.
- 73 ROSSI, B.; GREISEN, K. Cosmic ray theory. **Reviews of Modern Physics**, v. 13, n. 4, p. 241, 1941.
- 74 GAISSER, T.; HILLAS, A. Reliability of the method of constant intensity cuts for reconstructing the average development of vertical showers. **International Cosmic Ray Conference**, v. 8, p. 353, 1977.
- 75 MOLIERE, G. Theory of the scattering of fast charged particles. 2.Repeated and multiple scattering. **Zeitschrift für Naturforschung**, A3, p. 78, 1948.

- 76 KAMATA, K.; NISHIMURA, J. The lateral and the angular structure functions of electron showers. **Progress of Theoretical Physics Supplement**, v. 6, p. 93, 1958.
- 77 GREISEN, K. Cosmic ray showers. **Annual Review of Nuclear and Particle Science**, v. 10, p. 63, 1960.
- 78 MATTHEWS, J. A Heitler model of extensive air showers. **Astroparticle Physics**, v. 22, n. 5-6, p. 387, 2005.
- 79 ALVAREZ-MUÑIZ, J. et al. Hybrid simulations of extensive air showers. **Physical Review D**, v. 66, p. 033011, 2002. doi: 10.1103/PhysRevD.66.033011.
- 80 MONTANUS, J. An extended Heitler – Matthews model for the full hadronic cascade in cosmic air showers. **Astroparticle Physics**, v. 59, p. 4, 2014.
- 81 WERNER, K.; LIU, F. M.; PIEROG, T. Parton ladder splitting and the rapidity dependence of transverse momentum spectra in deuteron-gold collisions at the BNL relativistic heavy ion collider. **Physical Review C**, v. 74, p. 044902, 2006.
- 82 OSTAPCHENKO, S. Monte Carlo treatment of hadronic interactions in enhanced Pomeron scheme: QGSJET-II model. **Physical Review D**, v. 83, p. 014018, 2011.
- 83 LIPARI, P.; ENGEL, J.; GAISSER, T.; STANEV, T. Nucleus-nucleus collisions and interpretation of cosmic-ray cascades. **Physical Review D**, v. 46, n. 11, p. 5013, 1992.
- 84 AHN, E. J.; ENGEL, R.; GAISSER, T. K.; LIPARI, P.; STANEV, T. Cosmic ray interaction event generator SIBYLL 2.1. **Physical Review D**, v. 80, p. 094003, 2009.
- 85 FLETCHER, R. S.; GAISSER, T. K.; LIPARI, P.; STANEV, T. SIBYLL: an event generator for simulation of high energy cosmic ray cascades. **Physical Review D**, v. 50, n. 9, p. 5710, 1994.
- 86 RANFT, J. Dual parton model at cosmic ray energies. **Physical Review D**, v. 51, n. 1, p. 64, 1995.
- 87 BOPP, F. W.; RANFT, J.; ENGEL, R.; ROESLER, S. Antiparticle to particle production ratios in hadron-hadron and d-Au collisions in the DPMJET-III Monte Carlo model. **Physical Review C**, v. 77, n. 1, p. 014904, 2008.
- 88 FESEFELDT, H. **GHEISHA program**. Aachen, 1985. Technical report PITHA 85-02.
- 89 BLEICHER, M. et al. Relativistic hadron-hadron collisions in the ultra-relativistic quantum molecular dynamics model. **Journal of Physics G**, v. 25, p. 1859, 1999.
- 90 TÖRBJORN, S. Status of fragmentation models. **International Journal of Modern Physics A**, v. 03, p. 751, 1988.
- 91 KWIECINSKI, J.; MARTIN, A. Semihard QCD expectations for proton-(anti)proton scattering at CERN, Fermilab Tevatron, and the superconducting super collider. **Physical Review D**, v. 43, n. 5, p. 1560, 1991.
- 92 SJÖSTRAND, T.; VAN ZIJL, M. A multiple-interaction model for the event structure in hadron collisions. **Physical Review D**, v. 36, n. 7, p. 2019, 1987.

- 93 GRIBOV, L. V.; LEVIN, E. M.; RYSKIN, M. G. Semihard processes in QCD. **Physics Reports**, v. 100, n. 1-2, p. 1, 1983.
- 94 CLINE, D.; HALZEN, F.; LUTHE, J. High transverse-momentum secondaries and rising total cross sections in cosmic-ray interactions. **Physical Review Letters**, v. 31, n. 7, p. 1716, 1993.
- 95 GAISSER, T.; HALZEN, F. "soft" hard scattering in the teraelectronvolt range. **Physical Review Letters**, v. 54, n. 16, p. 1754, 1985.
- 96 PANCHERI, G.; SRIVASTAVA, Y. Low pt jets and the rise with energy of the inelastic cross section. **Physics Letters B**, v. 182, n. 2, p. 199, 1986.
- 97 DURAND, L.; HONG, P. QCD and rising cross sections. **Physical Review Letters**, v. 58, n. 4, p. 303, 1987.
- 98 CHATRCHYAN, S. et al. Measurement of pseudorapidity distributions of charged particles in proton-proton collisions at $\sqrt{s}=8$ TeV by the CMS and TOTEM experiments. **European Physical Journal C**, v. 74, p. 3053, 2014.
- 99 ANTCHEV, G et al. Measurement of elastic pp scattering at $\sqrt{s} = 8$ TeV in the coulomb-nuclear interference region – determination of the p parameter and the total cross-section. **European Physical Journal C**, v. 75, p. 126, 2016.
- 100 DRESCHER, H. J.; HLADIK, M.; OSTAPCHENKO, S.; WERNER, K. A unified treatment of high-energy interactions. **Journal of Physics G**, v. 25, p. L91, 1999.
- 101 LIU, F. M.; DRESCHER, H. J.; OSTAPCHENKO, S.; PIEROG, T.; WERNER, K. Consistent treatment of soft and hard processes in hadronic interactions. **Journal of Physics G**, v. 28, p. 2597, 2002.
- 102 GRIBOV, V. Strong coupling in the Pomeranchuk pole problem. **Soviet Physics**, v. 26, p. 414, 1968.
- 103 HLADIK, M.; DRESCHER, H. J.; OSTAPCHENKO, S.; PIEROG, T.; WERNER, K. Self-consistency requirement in high-energy nuclear scattering. **Physical Review Letters**, v. 86, n. 16, p. 3506, 2001.
- 104 OSTAPCHENKO, S. Cosmic ray interaction models: an overview. **EPJ Web of Conferences**, v. 120, p. 04003, 2016.
- 105 GORBUNOV, D. S.; RUBTSOV, G. I.; TROITSKY, S. V. Air-shower simulations with and without thinning: artificial fluctuations and their suppression. **Physical Review D**, v. 76, n. 4, p. 043004, 2007.
- 106 KOBAL, M. A thinning method using weight limitation for air-shower simulations. **Astroparticle Physics**, v. 15, n. 3, p. 259, 2001.
- 107 HILLAS, A. Shower simulation: lessons from MOCCA. **Nuclear Physics B**, n. 3, p. 29, 1997.
- 108 HECK, D. et al. **CORSIKA**: a Monte Carlo code to simulate extensive air showers. Forschungszentrum Karlsruhe, 1988. Technical report FZKA-6019.

- 109 BILLOIR, P. A sampling procedure to regenerate particles in a ground detector from a “thinned” air shower simulation output. **Astroparticle Physics**, v. 30, n. 5, p. 270, 2008.
- 110 GHIA, P. L. (on behalf of the Pierre Auger Collaboration). Statistical and systematic uncertainties in the event reconstruction and S(1000) determination by the Pierre Auger surface detector. In: INTERNATIONAL COSMIC RAYS CONFERENCE, ICRC, 29, 2005, Pune, India. **Proceedings**...Pune: ICRC, 2005. v. 00, p. 101.
- 111 ANTONI, T. et al. Muon density measurements with the KASCADE central detector. **Astroparticle Physics**, v. 16, n. 4, p. 373, 2002.
- 112 TODERO, C. J.; SOUZA, V.; BELLIDO, J. A. Comparison of the moments of the X_{max} distribution predicted by different cosmic ray shower simulation models. **Astroparticle Physics**, v. 47, p. 18, 2013.
- 113 BRUIJN, R.; SCHMIDT, F.; ILEE, J.; KNAPP, J. Study of statistical thinning with fully-simulated air showers at ultra-high energies analysis. In: INTERNATIONAL COSMIC RAYS CONFERENCE, ICRC, 31, 2009, Lodz, Poland. **Proceedings**...Lodz: ICRC, 2009. v. 2, p. 39.
- 114 ABRAHAM, J. et al. Properties and performance of the prototype instrument for the Pierre Auger Observatory. **Nuclear Instruments and Methods in Physics Research**:section A, v. 523, n. 1-2, p. 50, 2004.
- 115 ABU-ZAYYAD, T. et al. The energy spectrum of ultra-high-energy cosmic rays measured by the Telescope Array FADC fluorescence detectors in monocular mode. **Astroparticle Physics**, v. 48, p. 16, 2013.
- 116 AAB, A. et al. The Pierre Auger cosmic ray observatory. **Nuclear Instruments and Methods in Physics Research**:section A, v. 798, p. 172, 2015.
- 117 ABRAHAM, J. et al. The fluorescence detector of the Pierre Auger Observatory. **Nuclear Instruments and Methods in Physics Research**:section A, v. 620, n. 2, p. 227, 2010.
- 118 HERMANN-JOSEF, M. (for the Pierre Auger Collaboration). **The HEAT telescopes of the Pierre Auger Observatory status and first data**. v. 3, p. 153, 2011. Available from: <<https://arxiv.org/ftp/arxiv/papers/1107/1107.4807.pdf>>. Accessible at: 13 Dec.2016.
- 119 ABRAHAM, J. et al. Measurement of the energy spectrum of cosmic rays above 10×10^{18} eV using the Pierre Auger Observatory. **Physics Letters B**, v. 685, p. 239, 2010.
- 120 AAB, A. et al. Measurement of the cosmic ray spectrum above 4×10^{18} eV using inclined events detected with the Pierre Auger Observatory. **Journal of Cosmology and Astroparticle Physics**, v. 2015, n. 08, p. 049, 2015.
- 121 ABRAHAM, J. et al. Upper limit on the cosmic-ray photon flux above 10^{19} eV using the surface detector of the Pierre Auger Observatory. **Astroparticle Physics**, v. 29, n. 4, p. 243, 2008.

- 122 _____. An upper limit to the photon fraction in cosmic rays above 10^{19} eV from the Pierre Auger Observatory. **Astroparticle Physics**, v. 27, n. 2-3, p. 155, 2007.
- 123 _____. Upper limit on the diffuse flux of UHE tau neutrinos from the Pierre Auger Observatory. **Physical Review Letters**, v. 100, p. 211101, 2008.
- 124 ABREU, P. et al. A search for ultra-high energy neutrinos in highly inclined events at the Pierre Auger Observatory. **Physical Review D**, v. 84, p. 122005, 2011.
- 125 _____. Search for point-like sources of ultra-high energy neutrinos at the Pierre Auger Observatory and improved limit on the diffuse flux of tau neutrinos. **Astrophysical Journal**, v. 755, p. L4, 2012.
- 126 AAB, A. et al. Large scale distribution of ultra high energy cosmic rays detected at the Pierre Auger Observatory with zenith angles up to 80 degrees. **Astrophysical Journal**, v. 802, n. 02, p. 111, 2015.
- 127 _____. Depth of maximum of air-shower profiles at the Pierre Auger Observatory.ii. composition implications. **Astrophysical Journal**, v.D90, n. 12, p. 122006, 2014.
- 128 _____. **The Pierre Auger Observatory upgrade - preliminary design report**. , 2016. Technical report. Available from: <<http://arxiv.org/abs/1604.03637>>. Accessible at: 13 Dec.2016.
- 129 ANDRINGA, S.; CAZON, L.; CONCEIÇÃO, R.; PIMENTA, M. The muonic longitudinal shower profiles at production. **Astroparticle Physics**, v. 35, n. 12, p. 821, 2012.
- 130 AAB, A. et al. Muons in air showers at the Pierre Auger Observatory: measurement of atmospheric production depth. **Physical Review D**, v. 90, n. 1, p. 012012, 2014.
- 131 CAZÓN, L.; VÁZQUEZ, R. A.; WATSON, A. A.; ZAS, E. Time structure of muonic showers. **Astroparticle Physics**, v. 21, n. 1, p. 71, 2004.
- 132 CAZÓN, L.; VÁQUEZ, R. A.; ZAS, E. Depth development of extensive air showers from muon time distributions. **Astroparticle Physics**, v. 23, n. 4, p. 393, 2005.
- 133 ABREU, P. et al. Interpretation of the depths of maximum of extensive air showers measured by the Pierre Auger Observatory. **Journal of Cosmology and Astroparticle Physics**, v. 2013, n. 02, p. 026, 2013.
- 134 COLLICA, L. et al. Measurement of the muon production depths at the Pierre Auger Observatory. **European Physics Journal**, v. 131, n. 9, p. 301, 2016.
- 135 CAZON, L.; CONCEIÇÃO, R.; PIMENTA, M.; SANTOS, E. A model for the transport of muons in extensive air showers. **Astroparticle Physics**, v. 36, p. 211, 2012.
- 136 BAUS, C. **Cosmic ray Monte Carlo package**. 2016. Available from: <<https://web.ikp.kit.edu/rulrich/crmc.html>>. Accessible at: 13 Dec.2016.